Master Degree programme - Second Cycle *(D.M. 270/2004)* in Sciences and Technologies of Bio- and Nano-Materials

Final Thesis

Ab initio simulation and investigation of a novel Ta-doped Zirconia material.

Supervisor
Ch.mo Prof. Alvise Benedetti

Co-Supervisors
Prof. Piero Riello
Dr. Stefano Fabris

Graduand
Tommaso Francese
818936

Academic Year
2013/2014

Università
Ca'Foscari
Venezia

—

Ca' Foscari
Dorsoduro 3246
30123 Venezia

A mia Mamma, Papà e Ludovico.

Ab-initio materials modeling based on the Density Functional Theory is used to investigate the structural and electronic properties of a novel oxide material obtained by doping zirconium oxide (ZrO2 - zirconia) with Ta atoms. The material may have interesting applications in medical and electronic technologies. The work is motivated and driven by X-Ray Diffraction experiments (XRD), which measure the lattice parameters, atomic positions and space groups of these zirconia-based materials. The actual composition and structure of the powders are not known precisely. The Rietveld fit applied to the XRD data, taken at room temperature and pressure, shows that, by increasing the Ta doping from 0 to 12 %, the main structures found in the powder are Monoclinic (P21/c), Orthorhombic (Pca21), and Monoclinic(C2/c) at higher Ta concentration. The calculations are focused on the orthorhombic and monoclinic phases. It is experimentally demonstrated that at high doping percentage, Ta-doped orthorhombic zirconia is stable in a wide range of temperatures, after a synthesis that involve a thermal treatment in vacuum. Calculations provide insight into the thermodynamic and structural stability of the pure and Ta-doped oxides and predict the minimum-energy crystal structure of the orthorhombic phase. Moreover the results allow for the characterization of the electronic band structure of the material and on the effects of the point defects on the electronic properties. In particular, when Ta substitute for a Zr ion forming a point defect, there is the appearance of gap states, which may be of interest for technological electronic applications. The stabilization process might occur as the ion-ion substitution induces the generation of oxygen vacancies for charge compensation. The phase transition should be related to the amount of tantalum introduced and so to the amount of vacancies generated. The computed results will be useful for interpreting the existing measurements and for prompting new experiments that, on the basis of this new fundamental understanding, may better exploit the most interesting features of this new material.

Contents

List of Tables

List of Figures

Chapter 1

Introduction

1.1 Zirconium Dioxide

In the plethora of advanced ceramic materials, zirconium dioxide (Zirconia) covers one of the most important roles. It is one of the best refractive and corrosion-resistant materials used in metallurgy and as a thermal barrier coating in engines and high temperature fuel cells[1]. Further it shows excellent intrinsic physical and chemical properties, which include high melting temperature (2715°C), wear resistance, toughness, strength and hardness[2]–[6]. Thanks to its uniquely properties it is nowadays applied in a wide range of industrial and medical fields. Pristine zirconia exhibits three crystal polymorphs, depending on temperature treatment. The most stable phase is the *monoclinic*, space group P21/c. It exists until temperature is less than 1170°C. In this configuration, Zr is in a distorted sevenfold coordination while O atoms are either in fourfold or threefold coordination. At higher temperatures the crystal phase changes and becomes *tetragonal* with a space group P4$_2$/nmc. Zirconium atoms are surrounded by eight anions, but with two slightly different Zr-O distances. This phase is stable until a new upper temperature value is reached, exactly 2370°C. Further, the structure changes into a *cubic* phase, space group Fm-3m. Here Zr presents a perfect eightfold coordination. Oxygen atoms in the tetragonal and cubic phases are fourfold coordinated. Zirconia phase diagram is shown in Figure 1.1, and it displays the temperature values for which occur the phases transitions, as stated above[7].
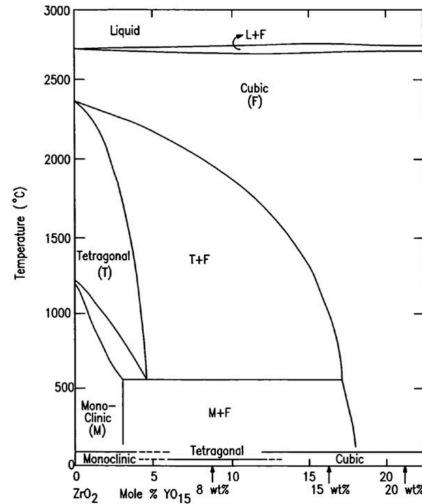
Figure 1.1: Phase diagram of zirconia

The fourth phase which is not listed in Figure 1.1 is the orthorhombic. This phase is frequently obtained applying high temperatures and pressures, which induce the distortion of the cubic crystal phase into an *orthorhombic*[8]–[12] one. Kudos *et al.*[13] have observed a such kind of structure on the basis of *in situ* single-crystal X-ray diffraction under pressure ranging from 3.9 to 5.1 GPa (39 and 51 kbar). In alternative an orthorhombic phase has been reported to form from the monoclinic phase under pressures greater than 3 GPa[14][15]. Furthermore, an orthorhombic phase can be freely produced in commercially high-toughness magnesia-partially stabilized zirconia (Mg-PSZ) by cooling to cryogenic temperatures[10][12][16]. It follows that the orthorhombic space group is not uniquely determined, but it can change as a function of pressure applied to zirconia powder or dopants introduced.

1.1.1 The Stabilization Problem

Obtaining stable sintered Zirconia samples is very difficult. The $t \rightarrow m$ transformation has been the subject of most careful attention, because it usually occurs during the sintering and on both heating and cooling. The lattice change is accompanied by a large shear strain and a large volume expansion, of about 9%. Together, these effects create large internal stresses on cooling, inducing sample cracking and disintegration[17].

Lattice transformations are *martensitic*: (1) being *diffusionless*, i.e. involving only coordinated shifts in lattice positions versus transport of atoms, (2) occurring *athermally*, implying the need for a temperature change over a range rather than at a specifics temperature and, (3) involving a *shape deformation*. Volume change on cooling associated with these transformations are substantial enough to make pristine material unsuitable for applications requiring intact solid structure[18].

Over the past 30 years many attempts were made to arrest the degradation processes correlated to ionic/vacancies diffusivity or volume expansion/decrease. The intent to dope zirconia with aliovalent cations or dopants is done with the aim to enhance some zirconia peculiar features. These might give rise to new materials able to evolve into new and more performant technologies. Different kinds of fully and partially stabilized zirconia materials were planned and used for a wide range of application until now, and the general classification is the following:

- for partial stabilized zirconia:

  - PSZ- Partially Stabilized Zirconia;

  - TSZ-Tetragonal Stabilized Zirconia;

  - 4YSZ-Partially Stabilized with 4 mol-% of Y_2O_3

- for fully stabilized zirconia:

  - FCZ-Fully Stabilized Zirconia;

  - CSZ-Cubic Stabilized Zirconia;

  - 8YSZ-Fully Stabilized with 8 mol-% of Y_2O_3

The difference between partial and fully stabilized zirconia depends upon the quantity of doping oxides used. Usually in fully stabilized zirconia the amount of dopant required is about 8 mol%, in the case of dopant Y_2O_3 with one oxygen vacancy created for every two yttrium ions [19]. The partial stabilization of tetragonal zirconia can occur at dopant concentrations of 2-5 mol% depending on grain size.

1.1.2 The Stabilization Mechanism

In the 70's, the ceramic engineering community was discovering that mixing zirconia with lower valence oxides, such as CaO, MgO, La_2O_3 and Y_2O_3, disfavored the strained monoclinic phase at room temperature and favored more symmetric metastable lattice structures, with * indicating metastability[21]. *Cubic** and *tetragonal** phases are analogous to those in pristine zirconia, but have dopant ions substituted on Zr^{4+} sites and have a fraction of oxygens sites vacant to retain charge[22]. Oxygen vacancies originate as a consequence to the introduction of cations or dopants, in order to maintain global charge neutrality. But these kind of defects can have a significant role in defining the functional and structural properties of ZrO_2 ceramics. Their concentration and spatial distribution are decisive factors in environmental stability and ionic diffusivity[19]. The real mechanism of zirconia stabilization is not fully understood, but some hypothesis have been proposed in recent years[19][20]. The recent theory distinguishes the phenomenon in two main areas as a function of oxygen hole concentration. In particular, when the concentration of vacancies is low, a relatively large volume of crystal is left into the fluorite structure and it undergoes to *tetragonal* distortion. The distortion not only involves all the oxygens, but also the atoms in defects proximity[20]. These take part to the distortion of the oxygen sublattice. On the other hand, when the defect concentration is high, the original cubic crystallographic shape is not maintained. Each oxygen site is either itself a neighbor of the vacancy site. It follows that there is no local regions which could undergoes to *tetragonal* distortion, because it has already taken place. The cubic shape arises only averaging over a wide number of atoms ≈ 100. Thus the stabilization process of $t*$ and $c*$ should be correlated just to the oxygen vacancies concentration and to the internal disorder which these create, rather than the dopants introduced[20]. Nevertheless dopants are needed to introduce the correct amount of oxygen and so vacancies into the bulk structure, and it depends upon metal ions valence state.

Yttria-doped zirconia is one of most studied compound and currently used material based on the zirconia doping process[23][24]. The yttrium oxide formula is Y_2O_3. So, replacing one Zr^{4+} lead to the generation of oxygen holes which, as explained above, should stabilize the bulk structure. In the same way, the introduction of the tantalia, Ta_2O_5, creates for each atomic unit the generation of one oxygen vacancy. In principle, as previously stated, it

should work the same stabilization mechanism. Nevertheless, it is unknown as which secondary effects could bring the tantalum in the zirconia matrix, and which kind of crystal structure could arise with doping and if they might be suitable in sintering technology.

1.1.3 Outlook

The focus of this work is the stabilization of orthorhombic zirconia phase by doping with *di*-tantalum pentoxide (Ta_2O_5). The thesis is organized as follow:

- In Chapter 2 we describe the idea which brought to dope zirconia with Ta_2O_5. The synthesis process used to obtain the new material and experimental results are presented. These data are the driven force of the Density Functional Theory investigation, as it will be explained later;

- In Chapter 3 we present the main theoretical aspects of the Density Functional Theory, ranging from the Thomas-Fermi model to Kohn-Sham equations to the definition of the Density of States and Bands Structure. It is a fundamental task to understand which are the basis of the algorithm used to simulate the doped structures and which are the advantages and limits of that;

- In Chapter 4 convergence tests are described with abundance of information. They represent a necessary step in the setting of the optimal parameters and approximations, implemented in pseudopotentials, used for simulating the crystal structures. The main aim of this part is to achieve the best compromise between speed of calculations and accuracy;

- Chapter 5 is dedicated to the reproduction of the main bulk structures under investigation. We compare the results with literature in order to verify the application of a method which has to be reproducible and reliable;

- In Chapter 6 the Atomistic *ab initio* Themodynamics theoretical approach is presented. It is the principal means that, on the basis of DFT calculations, predicts the Ta-doped zirconia thermodynamical behavior

with respect to pristine zirconia. We summarize all the main aspect of this work, results and predictions. Moreover we declared how work will prosecute and which might be the future developments and objectives. We evaluate the thermodynamical properties of Ta-doped zirconia and we use them to predict how the doping process could influence the bulk structure.

Chapter 2

Tantalia-Doped Zirconia

2.1 Motivations

While there is exhaustive literature[25]–[27] dedicated to describe the effects of divalent, e.g. Ca^{2+} or Mg^{2+}, trivalent, e.g. Y^{3+} or La^{3+}, and tetravalent, e.g. Hf $^{4+}$, ions in the zirconia matrix, on the other hand a few pentavalent ions are analyzed, Niobium and Vanadium[28][29]. Usually, the doping effect correlated to the introduction of pentavalent atoms like Nb^{5+}, Ta^{5+} and V^{5+} are thought to be unfavorable for stabilization of metastable polymorphs of ZrO_2 because of their charge and size[30]. Nevertheless tantalum(V)-doped nanocrystal of pure t-ZrO_2 from a chemical synthesis method have been already reported[31]. The synthesis of this material is pondered in the light of the fact that oxygen vacancy carrier properties of zirconia should be enhanced by the doping with Ta^{5+}, but it also might induce the formation of particular crystal shapes with unexpected properties.

2.2 Synthesis

The method used in the synthesis process is the *co*-precipitation. It is an easy and reliable method. It enables us to control the right size of particles dimensions, which are in the around of $\approx$ 100-600 nm. This is a fundamental aspect in Material Science and Engineering if the material has to be process after, e.g. sintering. Different steps have to be followed for obtaining Ta-doped zirconia, and virtually, every kind of compound we want to do with this process. These are referred to this particular material.

In a glass flask a solution of zirconium chloride 0.1 M, in EtOH:H_2O mixture 9:1, is added to a solution of tantalum chloride 0.0125 M in EtOH. 1.037 ml of NH_3 28% wt are dripped into the flask containing the solution above. Ammonia should be stoichiometrically in excess with respect to the zirconium chloride concentration. The pH should be in the around of 10 for all the reaction duration. This will guarantee the efficient precipitation of the oxide during the stirring process, that has to go ahead for 30 minutes. This ensures that the majority of Ta-doped zirconia powder precipitates. The powder obtained needs to be accurately washed with EtOH and distilled water for removing all the NH_3 remains. The risk is the possibility to have secondary reactions which can give rise to unwanted products. Finally the powder has to be dried. This is performed in two times: the first one is the removal of the large amount of water and it is usually done into a conventional oven at the temperature of 100°C. The second sequence is the true thermal treatment. It is carried out in vacuum into a high temperature oven, able to reach temperatures of about 1000°C. This is fundamental because it ensures that no solvent remains wedged into the powder structure, into pores or else. In this work different samples are synthesized. The amount of tantalum is made varying in the range between 1% to 12%. The different number of samples with different doping percentage are planned to be helpful in identifying particular phases which might raise thanks to doping effect. In the following table are listed the reagents used in the synthesis process.

Table 2.1: Reagents used and their purity. wt% refers to the percentage of compound which is dissolved into a water solution. Purity instead refers to the percentage amount of spurious elements which are present in the chemical solution. S.-A. means Sigma-Aldrich.

Reagent Name	Chemical Formula	wt% in H_2O	Purity %	Retailer
Yttrium-chloride·(6H_2O)	$YCl_3 \cdot 6H_2O$	***	99.99	S.-A.
Tantalum-chloride	$TaCl_5$	***	99.8	S.-A.
Zirconyl-chloride·(8H_2O)	$ZrOCl_2 \cdot 8H_2O$	***	98	S.-A.
Ammonia	NH_3	28	***	S.-A.
Ethanol	C_2H_6O	99.8	***	S.-A.

The list of the samples synthesized in this process can be seen in Table 2.2.

Each row in the table reports the moles per element used and the corresponding solution volume used.

Table 2.2: Ta-doped zirconia samples. It is shown the moles and volumes correlated to the doping performed. The oxygen moles are estimated on the basis of Eq. (2.1).

Samples	Zr [mol]	Volume [ml]	Ta [mol]	Volume [ml]	O [mol]
ZT-1%	0.990	49.5	0.010	4	1.995
ZT-3%	0.970	48.5	0.030	12	1.985
ZT-4%	0.960	48	0.040	16	1.980
ZT-4.5%	0.955	47.8	0.045	18	1.978
ZT-5%	0.950	47.5	0.050	20	1.975
ZT-8%	0.920	46	0.080	32	1.960
ZT-12%	0.880	44	0.120	48	1.940

The generalized chemical formula which is supposed to correlate the different amount of elements is:

$$Zr_{(1-x)}Ta_xO_{(2-\frac{x}{2})}$$
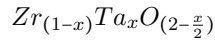
It currently does not describe correctly the real chemical structure of the Ta-doped zirconia because of the increasing in oxygen vacancy concentration as a function of increasing doping percentage.

2.3 XRD and Rietveld Refinement

X-Ray Powder Diffraction (XRD) is one of the most important characterization techniques in Material Science (MS). It is used for phase identification of crystalline material and it can provide information on unit cell dimensions. Max von Laue, in 1912, discovered that crystalline substances act as 3D diffraction gratings. It is a common technique for the study of crystal structures. XRD is based on constructive interference of monochromatic X-Rays with crystal lattices. X-Rays are generated by a cathode ray tube, conveniently filtered to produce monochromatic radiation. The radiation is collimated, concentrated and directed towards the sample under investigation. Constructive interference is produced when incident rays and sample atomic structure satisfy Bragg's Law:

$$n\lambda = 2d\sin\theta \tag{2.1}$$

This law relates the wavelength of electromagnetic radiation to the diffraction angle and lattice spacing in a crystalline sample. The diffracted X-Rays are then detected, processed by a computer and counted.

By scanning the sample through a range of 2θ angles, all possible diffraction directions of the lattice should be considered due to the random orientation of the powdered material. The conversion of the diffraction peaks to d-spacings allows identification of the crystallographic group and so the mineral to which the sample belongs to. This is possible because each mineral has a set of unique d-spacings. Generally, this is achieved by direct comparison with a reference pattern.

2.3.1 Experimental Synchrotron XRD Spectra

The Synchrotron Radiation Facility in Trieste is a very useful place to carry out experiments in MS. The whole machine depends on a physical phenomenon: when electrons change direction, they emit radiation.

The energy of each electron is inversely scaled with electron wavelength.

It means that as electron energy grows up, the wavelength associated to become shorter, and the emitted energy due to fast direction change become higher. So, the Synchrotron Facility is a great machine able to accelerate electrons to very high energetic trends and produce extremely collimated X-

Rays beams in the different beam lines, where scientists work. Each beam line is technologically organized in order to carry out a particular experiment and to take advantage of a fraction of the light source. Bragg's Law is valid in this context. There are two main differences from common X-Rays machines: the extremely high intensity and the elevated monochromaticity of radiation. In this context, *in situ* temperature Wide Angle X-ray Scattering (WAXS) experiments are done. The different samples synthesized are irradiated by synchrotron radiation in a temperature ramp. The aim of this particular experiment is to recognize the presence of an uncommon crystal phase or if the present phase in the sample has a variation at different temperature values.

Something unexpected it was found. The particular phase identified by Rietveld refinement is stable at every T values investigated. The following images not mince words:

(a) Tantalia-doped Zirconia:
doping at 3%

(b) Tantalia-doped Zirconia:
doping at 5%

(c) Tantalia-doped Zirconia:
doping at 8%
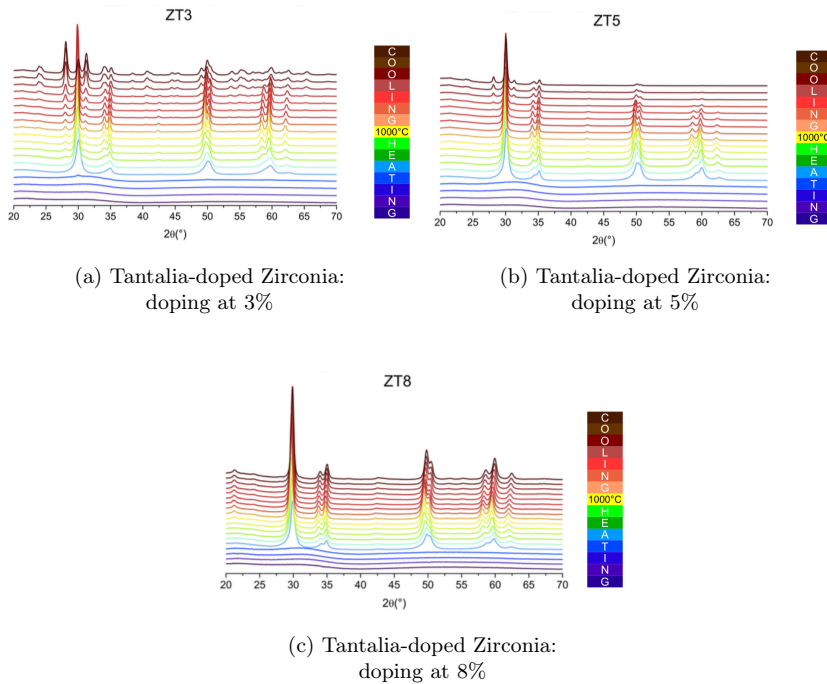
Figure 2.1: Different samples analysed at Synchrotron Radiation Facility in Trieste

In Figure 2.1 a,b and c, it can be seen the three different samples analyzed and their behavior in the temperature range up to 1200°C. The analysis of these particular samples with those particular Ta-doping percentage is a pondered choice: they are representative of the behavior of tantalum incorporated into the zirconia matrix and give an overview on how it modifies the crystal shapes as a function of T.

2.3.2   Thesis Goal

Differently from the others samples, Figure 2.1 c (labelled ZT8), shows that the spectra taken do not change during the thermal treatment, neither heating nor cooling. It means that the crystal structure is very stable, and it might be a suitable candidate in practical applications and devices. These data are the driving force which brought to the computational approach based on the DFT, in the attempt to clarify and to justify the stabilization mechanism of the orthorhombic phase. Insight into these fundamental issues can be provided by accurate material modeling. In the following work we investigate pure and Ta-doped zirconia materials and fully characterize their atomistic and electronic properties. We consider two main defects models. The resulting crystalline structure are forced to be electronically neutral.

Model 1): we substitute two zirconium atoms with two tantalum atoms., and generate one oxygen vacancy. In the Kröger-Vink notation is

$$2Ta^{\bullet}_{Zr} + 1V^{\bullet\bullet}_O + 4e^- = 0 \tag{2.2}$$

where Ta_{Zr} states for the zirconium replacement with a corresponding tantalum atom, V_O represent the oxygen vacancy, e$^-$ states for the electron negative charge, and black dots ($^{\bullet}$), $represent the positive charges that ensue from the doping.$

Model 2): we take into account the localization of electrons in the tantalum atoms proximity. In Kröger-Vink notation we can write

$$2Ta^{\bullet} + 2e^{-} \approx 2Ta^{4+} \qquad (2.3)$$
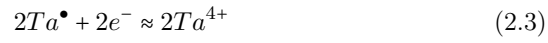
because tantalum atoms behave like pseudo-zirconiums, being their effective +5 valence charge shielded by the presence of the localized electron. These two models are considered and adapted to the crystalline Ta-doped zirconia structure investigated.

Chapter 3

Density Functional Theory: Basis

Density Functional Theory (DFT) provides the best compromise between accuracy and system size to simulate the properties of matter from first principles. It is a quantum-mechanical method used in physics, material science and chemistry to investigate the electronic structure of atoms, molecules and solids. The DFT method is based on *functionals*. A functional is a mapping of an entire function f to a resulting number F[f]; whereas a common function is defined to be a mapping of a variable x to a result (a number) *f(x)*. In DFT, the functional depends on the electron density. In 1964 Hohenberg and Kohn published a ground-breaking article[33], which lead to the development of (DFT). Hohenberg and Kohn showed that there exists a functional F[n] such that the ground state energy can be expressed as the minimum of the functional:

$$E_V\left[n\right] = F\left[n\right] + \int d\vec{r}\ V(\vec{r})\ n(\vec{r}) \tag{3.1}$$

where $n(\vec{r})$ is the charge-density, and F$[n]$ does not depend on the system. This fact makes it possible to describe, at least in principle, the ground state properties of the system of interacting electrons in terms of the charge-density only, rather than on the far more complicated many-particle wavefunction.

3.1 Thomas-Fermi Model

The original DFT method was developed by Thomas and Fermi in 1927. In spite of the fact that approximations used at that time were not so accurate as nowadays, the approach used in Thomas-Fermi model shows how DFT operate. The conventional approaches use the wavefunction Ψ as the central quantity, since Ψ contains the full information of the system. Nevertheless, Ψ is a very complex quantity that cannot be probed experimentally and that depends on $3N$ degrees of freedom, where N is the number of electrons. In Thomas-Fermi approach the kinetic energy of the system of electrons is approximated as an explicit functional of the density. Electrons are supposed to be in an ideal system, where they do not interact with each others, and they belong to an homogeneous gas with density equal to the local density at any given point. The kinetic energy functional proposed is:

$$T_{TF}\left[\rho(\vec{r})\right] = \frac{3}{10}(3\pi^2)^{\frac{2}{3}} \int \rho^{\frac{5}{3}}(\vec{r})d\vec{r} \tag{3.2}$$

The energy of an atom is finally calculated using the classical expression for the nuclear-nuclear potential and the electron-electron potential:

$$T_{TF}\left[\rho(\vec{r})\right] = \frac{3}{10}(3\pi^2)^{\frac{2}{3}} \int \rho^{\frac{5}{3}}(\vec{r})d\vec{r} - Z \int \frac{\rho(\vec{r})}{r}d\vec{r} + \frac{1}{2} \int \int \frac{\rho(\vec{r}_1)\rho(\vec{r}_2)}{r_{12}}d\vec{r}_1 d\vec{r}_2 \tag{3.3}$$

The energy is completely given in terms of electron density. In order to determine the correct density to be included in Eq. 3.3, Thomas and Fermi made use of a *Variational Principle*. They assumed that the ground-state of the system is connected to $\rho(\vec{r})$ for which the energy is minimized under the constraint of

$$\int \rho(\vec{r})d\vec{r} = N \tag{3.4}$$

3.1.1 Variational Principle in Ground State Configuration

If a system is in the state Ψ, the expectation value of the energy is given by

$$E\left[\Psi\right] = \frac{\left\langle \Psi \left| \hat{H} \right| \Psi \right\rangle}{\left\langle \Psi | \Psi \right\rangle} \tag{3.5}$$

where

$$\left\langle \Psi \left| \hat{H} \right| \Psi \right\rangle = \int \Psi^* \hat{H} \Psi d\vec{x} \qquad (3.6)$$

The V.P. states that the energy computed from a guessed Ψ is an upper bound to the true ground-state energy $E_0^{[32]}$. Full minimization of the functional $E[\Psi]$ with respect to all allowed N-electrons wavefunctions will give the true ground state Ψ_0 and energy $E[\Psi_0] = E_0$; so,

$$E_0 = min_{\Psi \rightarrow N} E[\Psi] = min_{\Psi \rightarrow N} \left\langle \Psi \left| \hat{T} + \hat{V}_{Ne} + \hat{V}_{ee} \right| \Psi \right\rangle \qquad (3.7)$$

For a system of N electrons and given nuclear potential V_{ext}, the V.P. defines a procedure to determine the ground-state wave function Ψ_0, the ground-state energy $E_0[N, V_{ext}]$, and other properties of interest[32]. In conclusion, the ground-state energy is a functional of the number of electrons N and the nuclear potential V_{ext}:

$$E_0 = E[N, V_{ext}] \qquad (3.8)$$

3.2 The Hohenberg-Kohn Theorems

3.2.1 Theorem I

The first Hohenberg-Kohn theorem[33] demonstrates that the electron density uniquely determines the Hamiltonian operator and thus all the properties of the system.

It states as follow[32]:

"*the external potential $V_{ext}(\vec{r})$ is, to within a constant, a unique functional of $\rho(\vec{r})$; since, in turn $V_{ext}(\vec{r})$ fixes $\hat{H}$, we see that the full many particle ground states is a unique functional of $\rho(\vec{r})$*"

Corollary I

Being the Hamiltonian fully determined, except for a constant shift of the energy, it follows that the many-body wavefunctions for all states, ground and excited, are determined. *Therefore all properties of the system are completely determined given only the ground state density $n_0(\vec{r})$.*

Proof

Let us assume the presence of two external potentials, $V_{ext}^{(1)}(\vec{r})$ and $V_{ext}^{(2)}(\vec{r})$, differing by more than a constant, each giving the same $\rho(\vec{r})$ for its ground state. We would have two Hamiltonians, $\hat{H}^{(1)}$ and $\hat{H}^{(2)}$, whose ground-state densities are the same, although the normalized wavefunctions $\Psi^{(1)}$ and $\Psi^{(2)}$ would be different. Since $\Psi^{(2)}$ is not the ground state of $\hat{H}^{(1)}$, it follows that:

$$E^1 = \left\langle \Psi^{(1)} \left| \hat{H}^{(1)} \right| \Psi^{(1)} \right\rangle < \left\langle \Psi^{(2)} \left| \hat{H}^{(1)} \right| \Psi^{(2)} \right\rangle \tag{3.9}$$

The rigorous inequality arises if the ground state is non-degenerate, that is taken into account here, following the Hohemberg and Kohn arguments. The last term in (3.9) can be written as follow:

$$\left\langle \Psi^{(2)} \left| \hat{H}^{(1)} \right| \Psi^{(2)} \right\rangle = \left\langle \Psi^{(2)} \left| \hat{H}^{(2)} \right| \Psi^{(2)} \right\rangle + \left\langle \Psi^{(2)} \left| \hat{H}^{(1)} - H^{(2)} \right| \Psi^{(2)} \right\rangle$$
$$= E^{(2)} + \int d^3r \left[V_{ext}^{(1)}(\vec{r}) - V_{ext}^{(2)}(\vec{r}) \right] n_0(\vec{r}) \tag{3.10}$$

so that

$$E^{(1)} < E^{(2)} + \int d^3r \left[V_{ext}^{(1)}(\vec{r}) - V_{ext}^{(2)}(\vec{r}) \right] n_0(\vec{r}) \tag{3.11}$$

Nevertheless, considering $E^{(2)}$ exactly in the same way, it will be found the same equations as above, with superscripts (1) and (2) interchanged:

$$E^{(2)} < E^{(1)} + \int d^3r \left[V_{ext}^{(2)}(\vec{r}) - V_{ext}^{(1)}(\vec{r}) \right] n_0(\vec{r}) \tag{3.12}$$

At this time, if we add together equations (3.11) and (3.12), we arrive at a contradictory inequality:

$$E^{(1)} + E^{(2)} < E^{(1)} + E^{(2)} \tag{3.13}$$

This brings us to the desired conclusion:
"*there cannot be two different external potentials differing by more than a constant which give rise to the same non-degenerate ground-state charge density. The density uniquely determines the external potential to within a constant*"

Since the Hamiltonian is uniquely determined, from the Corollary it follows that in principle, the wavefunctions of any state is determined by solving the Schrdinger equation with this Hamiltonian. Among all the solutions consistent with the given density, the unique ground-state wavefunction is the

one that has the lowest energy.

3.2.2 Theorem II

The second Hohenberg-Kohn theorem ensures that a certain density is the ground-state density that we are looking for.
It states as follow[32]: "$F_{HK}[\rho]$, *the functional that delivers the ground-state energy of the system, delivers the lowest energy if and only if the input density is the true ground-state density.*"
In other words, this is the *variational principle*:

$$E_0 \leq E\left[\tilde{\rho}\right] = T\left[\tilde{\rho}\right] + E_{Ne}\left[\tilde{\rho}\right] + E_{ee}\left[\tilde{\rho}\right] \tag{3.14}$$

Corollary II

It states that the only functional $E[\text{n}]$ is sufficient to determine the exact ground state energy and density.

Proof

The Hohenberg-Kohn original demonstration is restricted to densities $n(\vec{r})$ that are electrons ground state densities of the hamiltonian with the presence of the external potential V_{ext}. Since all properties are uniquely determined if $n(\vec{r})$ is specified, then each property can be viewed as a functional of $n(\vec{r})$. The total energy functional is included:

$$E_{HK}[n] = T[n] + E_{int}[n] + \int d^3 r V_{ext}(\vec{r}) n(\vec{r}) + E_{II} \tag{3.15}$$

where E_{II} is the nuclei energy interaction.
Equation 3.15 can be rewritten as

$$F_{HK}[n] + \int d^3 r V_{ext}(\vec{r}) n(\vec{r}) + E_{II} \tag{3.16}$$

where F_{HK} is the functional which includes all the internal energies, potential and kinetic, of the interacting electron system

$$F_{HK}[n] = T[n] + E_{int}[n] \tag{3.17}$$

Now consider a system with ground state density equal to $n^{(1)}(\vec{r})$ which correspond to the external potential $V_{ext}^{(1)}(\vec{r})$. It follows that the Hohernberg-Kohn functional is equal to the expectation value of the hamiltonian in the unique ground state, to whom belongs the wavefunction $\psi^{(1)}$

$$E^{(1)} = E_{HK}[n^{(1)}] = \left\langle \Psi^{(1)} \left| \hat{H}^{(1)} \right| \Psi^{(1)} \right\rangle \tag{3.18}$$

If a different density is now considered, labelled as $n^{(2)}(\vec{r})$, which corresponds to a different wavefunction $\Psi^{(2)}$, it follows immediately that $E^{(2)}$ of the last state examined is greater than $E^{(1)}$, and so

$$E^{(1)} = \left\langle \Psi^{(1)} \left| \hat{H}^{(1)} \right| \Psi^{(1)} \right\rangle < \left\langle \Psi^{(2)} \left| \hat{H}^{(2)} \right| \Psi^{(2)} \right\rangle = E^{(2)} \tag{3.19}$$

The meaning is the following: the Hohenberg-Kohn functional evaluated for the correct ground state density $n_0(\vec{r})$ is lower than the value of the previous expression for any other density $n(\vec{r})$.

Indeed Corollary II establishes that by minimizing the total energy of the system, with respect to variations in the density function $n(\vec{r})$, it could be found the exact ground state density and energy.

3.3 The Kohn-Sham Approach

In 1965 Kohn and Sham[34] proposed the revolutionary idea that made available the use of computational approach in condensed matter physics. The idea is the following: the substitution of the difficult interacting many-body system obeying the hamiltonian

$$
\hat{H} = -\frac{\hbar^2}{2m_e} \sum_i \nabla_i^2 - \sum_{i,I} \frac{Z_I e^2}{|\vec{r}_i - \vec{R}_I|} + \frac{1}{2} \sum_{i \neq j} \frac{e^2}{|\vec{r}_i - \vec{r}_j|} \\
- \sum_i \frac{\hbar^2}{2M_I} \nabla_I^2 + \frac{1}{2} \sum_{I \neq J} \frac{Z_I Z_J e^2}{|\vec{R}_I - \vec{R}_J|}
$$

(3.20)

where electrons are labelled by lower case subscript and nuclei, with charge Z_I and mass M_I, denoted by upper case subscripts, with a different *auxiliary system*. Such *system* can be solved because it is formed of a set of independent non-interacting systems. The Kohn-Sham *ansatz* assumes that the ground state density of the original interacting system is equal to that of the non-interacting systems. The KS *ansatz* is built upon two main assumptions:

1. the exact ground state can be described by the ground state density of the *auxiliary system* of non-interacting particles;

2. the auxiliary hamiltonian is chosen in order to have the usual kinetic operator and an effective *local* potential $V_{eff}^\sigma(\vec{r})$ acting on an electron of spin σ at point $(\vec{r})$. The local form is not essential, but it is a useful simplification which is considered as one of the KS equation main features.

The KS *ansatz* can be summarized in the following scheme[16]

$$
V_{ext}(\vec{r}) \quad \overset{HK}{\Longleftarrow} \quad n_0(\vec{r}) \quad \overset{KS}{\Longleftrightarrow} \quad n_0(\vec{r}) \quad \overset{HK_0}{\Longrightarrow} \quad V_{KS}(\vec{r})
$$

$$
\Downarrow \qquad\qquad \Uparrow \qquad\qquad \Uparrow \qquad\qquad \Downarrow
$$

$$
\Psi_i(\vec{r}) \quad \Rightarrow \quad \Psi_0(\vec{r}) \qquad\qquad \Psi_{i=1,N_e}(\vec{r}) \Leftarrow \Psi_i(\vec{r})
$$

where HK_0 represents the Hohenberg-Kohn theorem applied to the non-interacting problem.

The double arrow labeled with KS provides the connection in both direction between the many-body system and the non-interacting particle system; so that the arrows connect any point to any other point.

3.3.1 Kohn-Sham Equations

How the fundamental physical quantities of a real system are taken into consideration? The *ground-state density* of the interacting system is assumed to be equal to the ground-state of the non-interacting particle system. Instead the *kinetic energy* of the complex system is approximated by the kinetic energy of the auxiliary system. All the difficult many-body terms of $T[n]$ are incorporated into the exchange-correlation term, E_{xc}. From the HK theorems comparison, the expression of the total energy that enters in Eq. (3.16) is evaluated, according to KS approach, by the functional $F[n]$

$$F[n] = T_{KS}[n] + \frac{e^2}{2} \int \frac{n(\vec{r})n(\vec{r}')}{|\vec{r} - \vec{r}'|} dr dr' + E_{xc}[n] \qquad (3.21)$$

where $T[n]$ represents the kinetic energy of the *auxiliary system*, that is a functional of the ground-state density $n(\vec{r})$. The second term, instead, is the well-known expression for the Hartree energy in terms of the Hartree density and potential

$$E_{Hartree}[n(\vec{r})] = \frac{1}{2} \int dr v_H(\vec{r})n(\vec{r}) = \frac{e^2}{2} \int \frac{n(\vec{r})n(\vec{r}')}{|\vec{r} - \vec{r}'|} dr dr' \qquad (3.22)$$

All the many-body effects of exchange and correlation are grouped into the exchange-correlation energy $E_{xc}[n]$.
$E_{xc}[n]$[32] can be written in terms of the HK functional, Eq. (3.17), as

$$E_{xc}[n] = F_{HK}[n] - (T_s[n] + E_{Hartree}[n]) \qquad (3.23)$$

or in a more rigorous form

$$E_{xc}[n] = \langle \hat{T} \rangle - T_s[n] + \langle \hat{V} \rangle - E_{Hartree}[n] \qquad (3.24)$$

In Eq. (3.23) and Eq. (3.24) $[n]$ denotes a functional of density $n(\vec{r}, \sigma)$, which depends upon both position in space $\vec{r}$ and spin σ. Equation 3.24 explicitly shows that the functional E_{xc} is the difference of the kinetic and the internal interaction energies of the true interacting many-body system from those of the fictitious independent-particle system, the *auxiliary system*, with electron-electron interactions replaced by the Hartree energy.

Note

If the functional $E_{xc}[n]$ was known, solving the KS equations could lead to the exact ground-state density and energy of the many-body electron system. It practice the KS approach is a feasible method able to calculate the ground-state properties of the electron system.

3.3.2 Kohn-Sham in Plane Waves

The Bloch's theorem for a periodic lattice is efficiently exploited in order to express the one-electron wavefunction in terms of a Fourier expansion. This is possible thanks to the use of plane waves basis sets. Plane waves are not the only possible basis set that can be used, but it has several advantages for condensed matter. The use of plane waves has also the advantage of being mathematically simple and, in principle, complete. It completely spans the Hilbert space. Plane waves basis set have also the advantage of covering all space equally. The last thing is extremely important if one does not know *a priori* the form of the electronic wavefunction. Not only advantages brings the plane wave basis set. It might occur that some regions present the electron density equally distributed, while in others it is highly concentrated. Many efforts at achieving methods that linearly scale with system have concentrated upon localized basis set[37]-[39]. The Fourier expansion needs to be truncated in order to be used in practice. Plane waves coefficients have a kinetic energy $E_K = \frac{\hbar^2}{2m}|\vec{k} + \vec{G}|^2$ where $\vec{k}$ represents the wave vector and $\vec{G}$ is the reciprocal lattice vector. In order to achieve a finite basis set, a kinetic energy *cutoff* is introduced

$$E_{cutoff} = \frac{\hbar^2}{2m}|\vec{k} + \vec{G}|^2 \qquad (3.25)$$

The choice of the E_{cutoff} determines the truncation of the plane waves expansion at a particular $\vec{G}$. The KS equations assume a particular from in term of plane waves expansions

$$\sum_{G'} \left[\frac{1}{2}|\vec{k} + \vec{G}|^2 \sigma_{\vec{G}\vec{G}'} + V_{ion}(\vec{G} - \vec{G}') + V_H(\vec{G} - \vec{G}') \right] c_{i,\vec{k}+\vec{G}'} = \epsilon_i c_{i,\vec{k}+\vec{G}} \qquad (3.26)$$

The reciprocal space representation of kinetic energy is diagonal, where potentials are described in terms of Fourier components. In principle, secular

Eq.(3.26) could be solved diagonalizing the Hamiltonian matrix $H_{\vec{k}+\vec{G},\vec{k}+\vec{G}'}$. The matrix elements are given in brackets in Eq.(3.26). The size of the matrix is defined by the E_{cutoff} term. The energy value depends on the pseudopotential chosen in order to describe the atomic species, as it will discuss in Section 3.4.

3.4 Pseudopotentials

The Pseudopotential is a mathematical effective potential that mimics the effect of ionic nucleus and core electrons. It ensues that the Schrödinger equation contains a modified effective core potential term instead of the Coulombic potential term. In this way the core states are practically eliminated, and the valence electrons are described by pseudo-wavefunctions with significant fewer nodes. Thus, it allows to the pseudopotential to be accurately described by fewer Fourier coefficients, and so making the plane-wave basis set usable in practice. Smoothness and transferability are main properties which define if a pseudopotential is efficient for a particular atomic species or not. Pseudopotentials should be as *smooth* as possible in order to have a convenient plane waves expansion (small kinetic cutoff values). While the *transferable* (thus accuracy) property is correlated with the ability of the pseudopotential to produce pseudo-orbitals that are as close as possible to true orbitals outside the core region, for *all systems containing a given atom*[40], as illustrated in Figure 3.1:
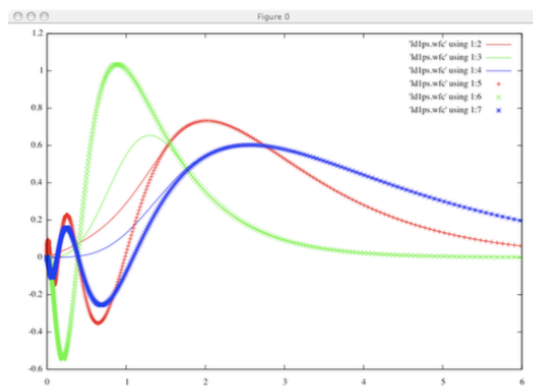
Figure 3.1: All-electrons and pseudo-orbitals functions for Si put in comparison.

Pseudopotential can be "shared" into two main categories, which will be described in Sections 3.4.1 and 3.4.2.

3.4.1 Norm-Conserving

The first point for defining the Norm-conserving pseudopotentials is the list of requirements for a good *ab initio* pseudopotential, as state in the paper

of D. R. Hamann, Schlüter and Chiang[41]:

1. Real and pseudo valence eigenvalues agree for a chosen "prototype" atomic configuration;

2. Real and pseudo atomic wave function agree beyond a chosen "core radius" r_c;

3. Integrals from 0 to r of the real and pseudo charge densities agree for $r > r_c$ for each valence state (norm-conservation);

4. The logarithmic derivates of the real and pseudo wave function and their *first energy derivatives* agree for $r > r_c$.

As a consequence of Point 1 and Point 2, it follows that the NCPP equals the atomic potential outside the "core regione" of radius r_c[32]. The potential is uniquely determined by the wavefunction and the energy ϵ, that does not need to be an eigenenergy. Point 3 requires that the integrated charge

$$Q_l = \int_0^{R_c} dr r^2 |\Psi_l(r)|^2 = \int_0^{R_c} dr \phi_l(r)^2 \qquad (3.27)$$

is the same for Ψ_l^{PS}, radial pseudo-potential, as for the all-electron radial orbital ψ_l, for a valence state. Q_l conservation ensures that:

- core regione total charge is correct;

- normalized pseudo-potential is equal to the true orbital outside of r_c;

Point 4 states that wavefunction $\Psi_l(\text{r})$ and its radial derivative $\Psi'_l(\text{r})$ are continuos at R_c, for any smooth potential. This last point contemplates a crucial step toward the aim of construct a "good" NCPP: it can be generated in a spherical atom, and then applied in a more complex system. It guarantees that the pseudopotential adapts as a function of the system to reproduce.

3.4.2 Ultrasoft

Ultrasoft pseudopotentials were first introduced by Vanderbilt[42] in 1990. As the name suggest, the idea of UPP is to relax the norm-conserving condition in order to generate much softer potentials. It follows that it can be used considerably fewer plane-waves for calculations of the same accuracy

as for NCPP. However, it is correlated to a little loss of *transferability*. In this scheme the pseudo-wave-functions are allowed to be as soft as possible within the core region, so that the cutoff energy can be reduced dramatically. Technically, this is achieved by introducing a generalized orthonormality condition. The electron density given by the squared moduli of the wave functions has to be augmented in the core region in order to recover the full electronic charge. The electron density is thus subdivided into:

- a) a smooth part that extends throughout the unit cell;

- b) a hard part localized in the core regions.

The augmented part appears in the density only, not in the wavefunctions. Ultrasoft PP have another advantage besides being much softer than the norm-conserving potentials. The USPP generation algorithm guarantees good scattering properties over a pre-specified energy range, which results in much better transferability and accuracy of pseudopotentials. USPP usually also treats "shallow" core states as valence by including multiple sets of occupied states in each angular momentum channel.
This also brings to high accuracy and transferability of the potentials, although at a price of computational efficiency.

Pseudopotentials Used in This Work

There are many sources of pseudopotential available on the web, for many different codes. In general these pseudopotentials are reliable, but they need to be tested for their performance in the system that will be simulated. In this work the pseudopotentials used are taken from the Quantum Espresso[43] web database. In particular here we describe each pseudopotential used, with an insight into its main features.
Zirconium ultrasoft pseudopotential, Zr.pbe-nsp-van.UPF, is generated with a scalar-relativistic calculation, using the Vanderbilt code, version 7.3.5. Being a transition metal, the pseudopotential is created from a (slightly) oxidized reference configuration to have improved transferability.

Table 3.1: Zirconium pseudopotential principal informations.

Pseudopotential Info					
Functional	PBE				
Valence Configuration	4S	4P	4D	5S	5P
Occupation	2.00	6.00	2.00	2.00	0.00
Z valence	12				
Tot. Energy [Ry]	-98.616311498				
Number of Wavefunction	5				
Number of Projectors	6				

As it can be seen in Table 3.1 only the last five electronic valence state are taken into consideration in the pseudopotential generation. The Z valence is the difference between the number of protons and core electrons and it is equal to 12. The exchange-correlation functional implemented is the PBE (Perdew-Burke-Ernzerhof)[44], which is a generalized gradient approximation, also known as GGA.
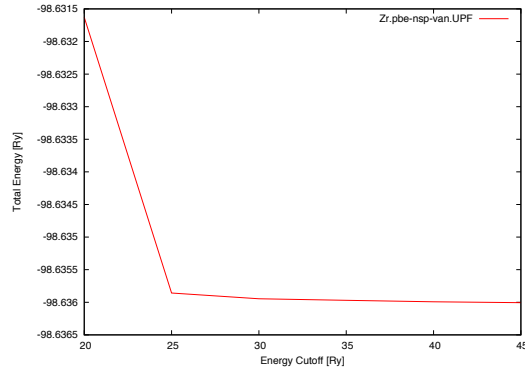
Figure 3.2: Convergence test for zirconium pseudopotential.

The convergence test depicts the trend which this pseudopotential has with respect to kinetic energy cutoff. Reaching a plateau at 25 Ry it means that this pseudopotential is well-performing for relative low energy cutoff

values. The *transferability* needs to be tested as it is used to reproduce crystal structures and compare the results with literature.

The necessity to use the same exchange-correlation functional implemented into zirconium pseudopotential, is extended also to tantalum and oxygen pseudos. Table 3.2 lists the main feature which describe the tantalum pseudo, following the same approach of the previous one. Valence states electronic configurations are listed, with the relative occupations.

Table 3.2: Tantalum pseudopotential principal informations.

Pseudopotential Info					
Functional	PBE				
Valence Configuration	5S	5P	5D	6S	6P
Occupation	2.00	6.00	3.00	2.00	0.00
Z valence	13				
Tot. Energy [Ry]	-141.34524077818				
Number of Wavefunction	5				
Number of Projectors	6				

Differently from zirconium, tantalum Z valence, the difference between protons and electrons, is equal to 13.
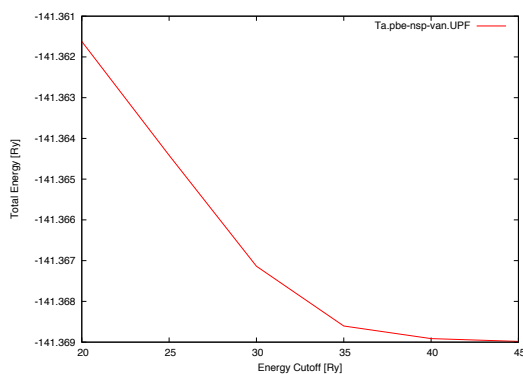
Figure 3.3: All-electrons and pseudo-orbitals functions for Si put in comparison.

Figure 3.3 shows instead the convergence trend which the tantalum pseu-

dopotential has. It can be seen that, differently from the zirconium pseudopotential, the trend tends to rapidly decade, but only at values above 30 Ry. It means that if the cutoff is wrongly set, the calculation will reach convergency with difficulty.

Finally, the last pseudopotential used is the that referred to oxygen. Oxygen is quite delicate to be treated in the DFT approach, due to its triplet electronic state. What follows is that if not correctly set and monitored, the calculation could not reproduce the correct electronic configuration. This task will be carefully taken into account in the atomistic *ab initio* thermodynamic calculations, where the total energy of oxygen atom and molecule are needed. Oxygen pseudopotential is in the PBE approximation. The number of electrons in valence considered (Z valence) are six.

Table 3.3: Oxygen pseudopotential principal informations.

Pseudopotential Info		
Functional	PBE	
Valence Configuration	2S	2P
Occupation	2.00	4.00
Z valence	6	
Tot. Energy [Ry]	-31.58339463984	
Number of Wavefunction	2	
Number of Projectors	4	

Figure 3.4 is of particular interest because it shows that the pseudo tends to reach convergence quite slowly; the plateau is not well defined as for those of zirconium or tantalum.

Nevertheless the cutoff at 30 Ry is sufficient to have a good compromise between accuracy and calculations speed.
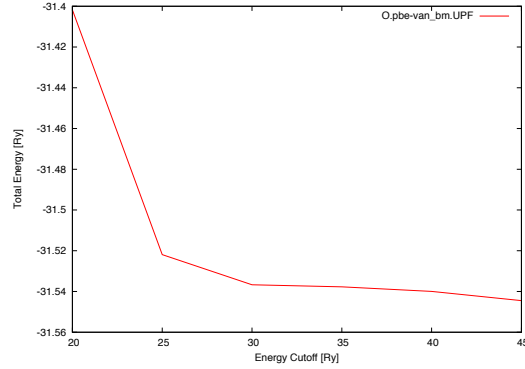
Figure 3.4: All-electrons and pseudo-orbitals functions for Si put in comparison.

As previously declared, it is essential to have the same kind of functional implemented in the pseudopotential used, otherwise it could lead to errors in the calculations, due to the different kind of approximations implemented. The GGA approximation depends upon the local density and its *local gradient*[40] $|\nabla n(\vec{r})|$,

$$E_{xc} = \int n(\vec{r}) \epsilon_{GGA}\left(n(\vec{r}), |\nabla n(\vec{r})|\right) dr \qquad (3.28)$$

In general the GGA functional class tends to correct the over-binding of LDA ("Local Density Approximation").

3.5 DFT in Pseudopotential Plane-Waves Framework

3.5.1 Basis Set

In a periodic system the potential presents the following property

$$V(\vec{r} + n\vec{a}) = V(\vec{r}) \tag{3.29}$$

where $\vec{r}$ and $\vec{a}$ are lattice vectors and n is an integer. The Bloch's theorem, implies that the wavefunctions can be written as a product of a periodic cell part and a wavelike part

$$\Psi_i(\vec{r}) = e^{i\vec{k}\vec{r}} f_i(\vec{r}) \tag{3.30}$$

$f_i(\vec{r})$ can be expanded as a set of plane waves

$$f_i(\vec{r}) = \sum_{\vec{G}} c_{i,\vec{G}} e^{i\vec{G}\vec{r}} \tag{3.31}$$

where $\vec{G}$ represent the reciprocal lattice vectors. So, the electronic wavefunction can be rewritten as

$$\Psi_i(\vec{r}) = \sum_{\vec{G}} c_{i,\vec{G}} e^{i(\vec{k}+\vec{G})\vec{r}} \tag{3.32}$$

Theoretically, an infinite number of basis function would be needed to exactly rebuilt the real wavefunction. Unfortunately it is not possible, and the expansion needs to be truncated. This is equivalent to impose a cutoff to the kinetic energy, being the kinetic energy of an electron define as

$$E_{\vec{k}} = \frac{\hbar^2 |\vec{k}|^2}{2m} \tag{3.33}$$

The kinetic energy cutoff brings an error in the total energy of the system, but in principle it can be controlled and reduced by increasing the size of the basis set. It is pursued incrementing the energy cutoff value. It finally permits to apply the KS equation as defined in Eq. (3.26), in Section 3.3.2 . Moreover, plane waves basis sets present other advantages with respect to Slater or Gaussian functions, and these include:

- the same basis set can be applied to different atomic species;

- plane waves do not depend on nuclear positions. It follows that correction terms are not needed for the forces calculation;

- the convergence *vs.* completeness can easily be tested.

3.5.2 Brillouin Zone Integration

Looking at the transition from non-periodic to periodic systems, one can realize that some important quantity become integrals of the Brillouin zone. For example, the sum of occupied eigenvalues

$$\sum_n \int_{BZ} d^3k \left[f_{n,\vec{k}} \cdot \epsilon_{n,\vec{k}} \right] \tag{3.34}$$

which contains the kinetic energy $T_s[\text{n}]$, or the density

$$n_0(\vec{r}) = \begin{cases} \sum_i f_i |\psi_i(\vec{r})^2| & \textbf{(non-periodic)} \\ \sum_n \int_{BZ} d^3\vec{k} \left[f_{n,\vec{k}} \cdot |\phi_{n,\vec{k}}(\vec{r})|^2 \right] & \textbf{(periodic)} \end{cases} \tag{3.35}$$

i defines the states of a non-periodic system, f_i and $f_{n,\vec{k}}$ denote the occupations numbers in a non-periodic and periodic systems, respectively. To obtain the density and total energy, it is necessary to solve continuos integral at, theoretically, infinitely many $\vec{k}$-points. These are localized in a single unit cell of the reciprocal space.

It needs to introduce another approximation: to solve the resulting integrals, discretizing $\vec{k}$-space to a few $\vec{k}$-points only, and to rewrite the integrals approximately as a weighted sum

$$\sum_n \int_{BZ} d^3k \; F(\vec{k}) \rightarrow \sum_{\vec{k}} \left[\omega(\vec{k}) \cdot F(\vec{k}) \right] \tag{3.36}$$

The evaluation of this expression is related to Brillouin zone sampling of a "few" $\vec{k}$-points, finding their integration weights, and then evaluating the KS equations only at these chosen $\vec{k}$-points. The simplest manner to achieve this purpose is an even-spaced integration grid of $\vec{k}$-points along the directions of the reciprocal lattice vectors. Figure 3.5 shows a two-dimensional example for the reciprocal-space unit cell of a hexagonal lattice.
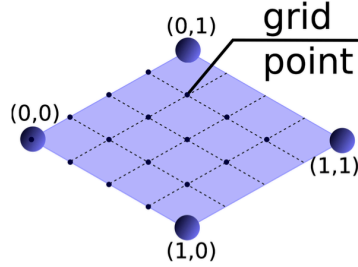
Figure 3.5: Reciprocal-space unit cell of a 2D hexagonal lattice. Large blue dots are the reciprocal lattice vectors, while the small define an even-spaced k-point integration grid that covers the unit cell.

In this example it is chosen the following $\vec{k}$-point integration grid (small blue dots)

$$\vec{k}(s_1, s_2, s_3) = \left(\frac{s_1}{n_1}\right) \cdot \vec{G}_1 + \left(\frac{s_2}{n_2}\right) \cdot \vec{G}_2 + \left(\frac{s_3}{n_3}\right) \cdot \vec{G}_3 \qquad (3.37)$$

where $\vec{G}_l$ represents the reciprocal lattice vectors, while s_i are integers in the limit $0 \leq s_i \leq n_i$. What is needed to do in practice, in a common DFT calculation, is to choose the integers n_1, n_2, n_3. This mathematical scheme yields an even-spaced $\vec{k}$-point grid, with uniform weights $\omega(\vec{k})$ and a sum of n_1, n_2, n_3 points.
The $\vec{k}$-point mesh needs however to be tested, depending on the system under investigation, in order to achieve the best compromise between calculation speed and accuracy.

3.5.3 Density Calculation

One of the most important quantities calculated in DFT is the calculation of electrons density, n. The general form used to describe it is

$$n(\vec{r}) = \frac{1}{N_{\vec{k}}} \sum_{\vec{k},i} f(\epsilon_{i,\vec{k}}) n_{i,\vec{k}}(\vec{r}) \tag{3.38}$$

where $n_{i,\vec{k}}(\vec{r}) = |\Psi_{i,\vec{k}}(\vec{r})|^2$. Eq.(3.38) is an average over $\vec{k}$-points, where i indicates the bands at each $\vec{k}$-point, and $f(\epsilon_{i,\vec{k}})$, which defines the occupations of the electron states. In a plane wave basis set, thanks to the Bloch functions, it can be written

$$n_{i,\vec{k}}(\vec{r}) = \frac{1}{\Omega} \sum_{m,m'} c_{i,m}^*(\vec{r}) c_{i,m'}(\vec{r}) e^{i(\vec{G}_{m'} - \vec{G}_m) \cdot \vec{r}} \tag{3.39}$$

and

$$n_{i,\vec{k}}(\vec{G}) = \frac{1}{\Omega} \sum_{m} c_{i,m}^*(\vec{k}) c_{i,m''}(\vec{k}) \tag{3.40}$$

where m'' denotes the $\vec{G}$ vector for which $\vec{G}_{m''} \equiv \vec{G}_m + \vec{G}$. To find all the Fourier coefficient requires a double sum, i.e. a convolution in Fourier space that requires N_G^2 operations, where N_G is the number of $\vec{G}$ vectors needed to describe the density. For large systems it becomes extremely expensive. The expedient is to use a fast Fourier transform (FFT). It allows one to transform from one space to the other in $N \log N$ operations, where $N = N_R = N_G$. The advantage is that $n(\vec{r})$ is needed to find $\epsilon_{xc}(\vec{r})$ and $V_{xc}(\vec{r})$. It is relevant to notice that the density n requires Fourier components, that extend twice as far in each direction as those needed for the wavefunction ψ because $n \propto |\psi|^2$. FFT needs a regular mesh in the form of a parallelepiped, in contrast with the fact that wavefunction cutoff is a sphere with $\left(\frac{1}{2}\right) |\vec{k} + \vec{G}|^2 < E_{cutoff}$. The FFT approach is much more efficient for large systems since the number of operations scales as $N \log N$.

3.5.4 Density of States

The *Density of States* (DOS) of a system describes the number of states, at each energetic level, which are available to the electrons. The DOS of a energetic level E is the number of energetic levels, between E and $E + dE$.

Per unit of energy the DOS is defined as follow:

$$DOS(E) = \frac{1}{N_{\vec{k}}} \sum_{i,\vec{k}} \delta(\epsilon_{i,\vec{k}} - E) \qquad (3.41)$$

while the DOS per unit of volume Ω in extended systems

$$DOS(E) = \frac{\Omega_{cell}}{(2\pi)^d} \int_{BZ} dk \; \delta(\epsilon_{i,\vec{k}} - E) \qquad (3.42)$$

In the independent-particle states, the equations above represent the number of independent-particle states per unit energy, where $\epsilon_{i,\vec{k}}$ denotes the energy of an electron. The density of states can be easily obtained once the molecular orbitals or, in a periodic system, the crystalline orbitals, are calculated. This is a powerful means which lets graphically visualize if the material under investigation is an insulator, rather than a conductor or semi-conductor.

3.5.5 Band Structure

The Schrödinger equation is:

$$H_{1e}\phi_n(\vec{r}) = \left(\frac{\vec{p}^2}{2m} + V(\vec{r})\right)\phi_n(\vec{r}) = E_n\phi_n(\vec{r}) \qquad (3.43)$$

where H_{1e}, $\phi_n(\vec{r})$ and E_n are, respectively, the one-electron Hamiltonian, the wavefunction and the energy of an electron in an eigenstate labeled n. Each eigenstate can be occupied at least by two electrons with opposite spin, (*Pauli's exclusion principle*).

When a particle moves in a periodic potential its wavefunctions can be expressed through the already cited *Bloch Functions*.

An eigenfunction $\phi(\vec{x})$ of H_{1e} can be expressed as a sum of Bloch functions:

$$\phi(\vec{x}) = \sum_{\vec{k}} A_{\vec{k}}\phi_{\vec{k}}(\vec{x}) = \sum_{\vec{k}} A_{\vec{k}}e^{(i\vec{k}\vec{x})}u_{\vec{k}}(\vec{x}) \qquad (3.44)$$

where $A_{\vec{k}}$ are constants. The one-electron wavefunctions can be labelled by constant $\vec{k}$, which are the wave vectors of the plane waves forming the "skeleton" of the Bloch function. In conclusion, a plot of the electron energies versus $\vec{k}$ is known as **Electronic Band Structure**. Bands structure plot in which $\vec{k}$ is allowed to vary over all possible values is known as the *extended*

zone scheme. Another way of choosing $\vec{k}$, which is more convenient and preferably used, is the so called *reduced zone scheme.* Thanks to translation property, $\vec{k}$ can be replaced by $\vec{k}' = \vec{k} - (2n\pi/R)$, where n is an integer chosen to limit $\vec{k}'$ to the interval $[-\pi/R, \pi/R]$.

This "enclosed" place is called IBZ.

Another fundamental means which help in terms of definition of the Bands Structure is the *Group Theory.* The approach of the GT will no longer be discussed here in its entirely mathematical aspects, but it is going to be explained "conversationally" just as an overview.

Group Theory is a mathematical branch which studies the so called *Groups*, where a *group* is an algebraic structure characterized by an associative binary operation, equipped with a neutral element, for which every element belonging to the structure owns an invert element. Various physical systems, such as crystals and the hydrogen atom, can be modeled by symmetry groups. Band structure diagrams are like maps and the group theory notations are like symbols on the map. Understanding symbols means exploring the electronic properties of the material under investigation.

Wavevectors take on any value inside the BZ, which is a polyhedron in wavevector space that is related to the crystal lattice. Wavevectors outside the BZ simply correspond to states that are physically identical to those states within the BZ. Special high symmetry points in the BZ are labelled like Γ, Δ, Σ. In scientific literature it is common to see bands structure plots which show the values of $E_n(\vec{k})$ versus different values of $\vec{k}$ along straight lines connecting symmetry points.

Energy band gaps are classified using the wave vectors of the states surrounding the band gap:

- **Direct Band Gap**: the lowest-energy state above the band gap has the same $\vec{k}$ as the highest-energy state below the band gap;

- **Indirect Band Gap**: the closest states above and below the band gap do not have the same $\vec{k}$ value.
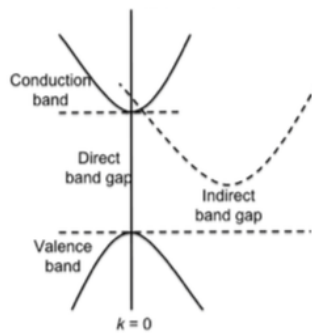
Figure 3.6: Direct and Indirect band gap scheme.

Chapter 4

Accuracy and Convergency Tests

4.1 Convergence Tests

The aim of the convergence tests is to study the best setting of the fundamental parameters useful to obtain a correct compromise between accuracy and speed of calculations. Moreover, the pseudopotentials for the different atomic species are checked in order to have a *good* representation of the bulk structure which will be investigated.

In the very first part of this work, the convergence achieved by an FCC zirconia system is tested. The software which performs the calculation is the Quantum Espresso[45]. The QE code is an integrated suite of Open-Source computer codes for electronic structure calculations and materials modeling at the nanoscale. The QE distribution consists of a "historical" core set of components, and a set of plug-ins that perform more advance tasks. It uses the *Density Functional Theory* approach, in plane-wave basis set.

4.1.1 Face-Centered-Cubic (FCC) Zirconia

At the beginning the system investigated should be as much simple as possible in order to easily evaluate the goodness of parameters in comparison with literature[46]. The atomic species and positions of the FCC zirconia structure are listed in the Table 4.1.

Table 4.1: Experimental atomic coordinates of cubic FCC zirconia structure.

Atomic Label	Coordinate (x)	Coordinate (y)	Coordinate (z)
Zr	0	0	0
O	0.25	0.25	0.25
O	0.75	0.75	0.75

The data have been extrapolated from a Rietveld fit refinement from X-Ray Powder Diffraction. A 3D model of the FCC Zirconia, Figure 4.1, is shown here. This structure is used as principal instrument for the self-consistency testing, thanks to its ease geometry.
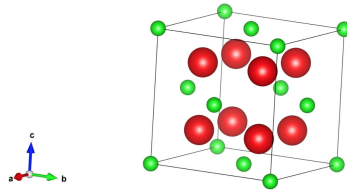
Figure 4.1: Zirconia FCC model: green spheres refers to the Zirconium while the red ones to the Oxygen.

The unit cell contains four zirconia (ZrO_2) units. Zr^{4+} and O^{2-} ions occupy the octahedral sites, as shown above, but, due to Zr:O ratio, half of the tetrahedral sites are filled by O^{2-}.

4.1.2 Work Plan

The first series of calculation is performed in order to establish which are the best lattice parameters values to be used in future calculations.
The tests are planned as follow:

- 1) on the basis of the experimental measure of the lattice parameters, a series of values, very close to the experimental one, are chosen. This is done for sampling the not so different structures that could be in the around of the experimental one;

- 2) the choice of the pseudopotential plays a fundamental role in the accuracy and performance of the calculations, as stated in Section 3.4;

- 3) in a simple script (see *Appendix A.2*), two variables, *lattice parameters* and $\vec{k}$-*point* sampling, are made varying at the same time: this ensures to obtain all the possible combinations and to optimise time and resources. It is fundamental to adequately organize the work in order to maximize the analysis of a huge amount of data that arises from these type of calculation;

- 4) once the output files are obtained, plotting on the same graph the total energy variation for the same $\vec{k}$-point sampling for different lattice parameters with respect to the variation of the lattice parameters let us visualize which is the range in atomic units around which it has to be perform a more punctual analysis. It can be seen in Figure 4.2 an example of the plot described.
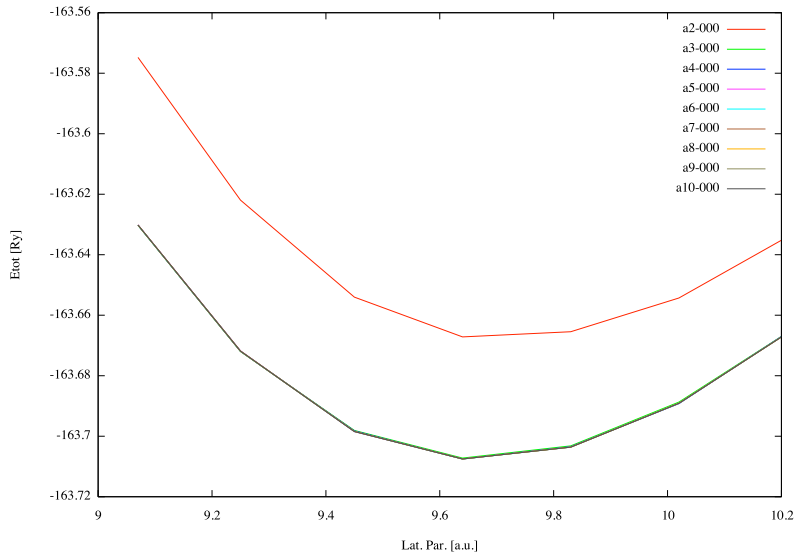
Figure 4.2: Total Energy *vs.* Lattice parameters variation. The origin grid offset for this series of calculation is at the origin 0 0 0.

- 5) being just an indicative perception of the best settings, the data gained from the previous calculation should be fitted with an *Equation Of State*. The chosen equation, for this work, is the Murnaghan EOS. In this way it can be compared not just the trend variation of the lattice

parameter but also the Bulk Modulus, Volume Energy and Enthalpy (see *Appendix A.1*).

The Murnaghan's EOS has the following form:

$$E(V) = E_0 + K_0 V_0 \left[\frac{1}{K_0'(K_0' - 1)} \left(\frac{V}{V_0} \right)^{1 - K_0'} + \frac{1}{K_0'} \frac{V}{V_0} - \frac{1}{K_0' - 1} \right] \qquad (4.1)$$

where K_0 is the modulus of incompressibility, K_0' is the first derivative of K_0 with respect to the pressure, V is the final volume, V_0 is the volume not compressed, and P is the pressure as a function of the volume. If the reduction of volume under compression is low, i.e. for $\frac{V}{V_0}$ greater than about 90%, the Murnaghan equation can model experimental data with satisfactory accuracy.

An example of a fitted curve is the following:
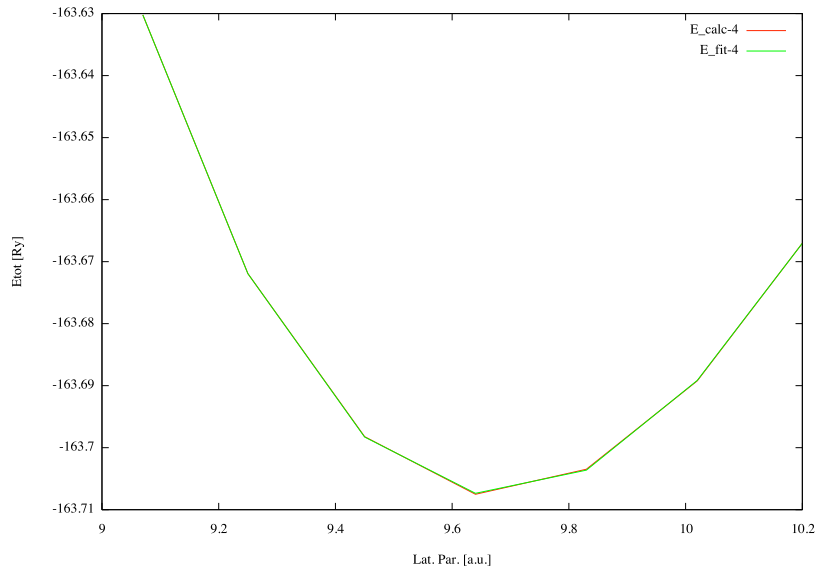
Figure 4.3: The fitting process is extremely supportive with the calculated data. The red line represents the calculated total energy in Rydberg with respect to the lattice parameter in atomic units. The green line is, instead, the Murnaghan's EOS fit. They are overlapped.

4.1.3 Setting the $\vec{K}$-Point Grid and Plane Wave Cutoff

In order to set the optimal values for the computational parameters, controlling the representation of the wavefunctions and the integrals in the Brillouin zone, we have used the following approach. First we set the kinetic energy cutoff (*ecutwfc*) to a large value, 40 Ry ($\approx$ 544.2 eV), and we explore the convergence of the structural parameters as a function of the $\vec{k}$-point grid. The results are listed in Table 4.2.

Table 4.2: Results data fitted for a different K-Points sampling

$\vec{K}$-Points sampling	Lat. Par. fit [a.u.]	Bulk Modulus [GPa]	Volume [a.u.]^3	E_{min} [Ry]
2x2x2	9.673	231.3	229.860	-163.66780
3x3x3	9.672	229.7	226.207	-163.70723
4x4x4	9.674	231.3	226.369	-163.70757
5x5x5	9.674	231.5	226.349	-163.70764
6x6x6	9.674	231.4	226.348	-163.70764
7x7x7	9.674	231.3	226.367	-163.70761
8x8x8	9.673	231.1	226.316	-163.70760
9x9x9	9.673	231.1	226.307	-163.70761
10x10x10	9.673	231.3	226.328	-163.70762

The fit carried out with the Murnaghan EOS allowed for the extrapolation of the bulk modulus, volume and energy minimum. The sampling of the Brillouin Zone is done with a grid offset centered in the origin. In order to be as precise as possible we focus on the rigid around of the minimum gained from the previous fitting, Table 4.3.

Thus a new cycle of calculations are performed in order to precisely find out not only the minimum-energy lattice parameters, but also to increase the precision of the bulk modulus.

Table 4.3: Data comparison for the calculation of the Lattice Parameters refinement at the origin.

$\vec{K}$-Points sampling	Lat. Par. fit [a.u.]	Bulk Modulus [GPa]	Volume [a.u.]^3	E_{min} [Ry]
2x2x2	9.707	213.5	228.717	-163.66781
3x3x3	9.667	208.3	225.886	-163.70734
4x4x4	9.673	234.4	226.296	-163.70772
5x5x5	9.671	237.9	226.180	-163.70771
6x6x6	9.673	255.1	226.318	-163.70775
7x7x7	9.671	242.2	226.176	-163.70773
8x8x8	9.671	231.5	226.187	-163.70772
9x9x9	9.671	228.4	226.153	-163.70769
10x10x10	9.671	231.1	226.166	-163.70770

We also considered shifted grids, which gave similar results, as it can be seen in Table 4.4. It is important to have under control the maximum number of variables, but also to minimize their degrees of freedom.

Table 4.4: Data comparison for the calculation of the Lattice Parameters shifted from the origin

$\vec{K}$-Points	Lat. Par. fit [a.u.]	Bulk Modulus [GPa]	Volume [a.u.]^3	E_{min} [Ry]
2x2x2	9.667	231.8	225.860	-163.71285
3x3x3	9.673	231.5	226.331	-163.70798
4x4x4	9.673	231.1	226.294	-163.70763
5x5x5	9.674	231.2	226.336	-163.70762
6x6x6	9.673	231.3	226.325	-163.70763
7x7x7	9.674	231.4	226.336	-163.70763
8x8x8	9.673	231.4	226.327	-163.70763
9x9x9	9.673	231.4	226.335	-163.70763
10x10x10	9.673	231.4	226.331	-163.70763

The sampling of the Brillouin Zone is shifted from the origin. In exact terms, the grid offset is displaced by half a grid step in each direction.

Having established that the 4x4x4 $\vec{k}$-point mesh is sufficient to converge the lattice parameters to 99.4%, the bulk modulus to 91.4% and the total energy to 99.9%, we now fix this grid ad explore the variation of these data with respect to the basis set cutoff. For doubt's sake we also considered a 6x6x6 mesh. The data are reported in Table 4.5.

Table 4.5: Comparison between two different BZ sampling

Cutoff [Ry]	Lat.Par. fit [a.u.]		Bulk Modulus [GPa]		Volume [a.u.]^3	
	4x4x4	6x6x6	4x4x4	6x6x6	4x4x4	6x6x6
20	9.3539	9.7166	149.1	227.7	204.605	229.341
25	9.6439	9.6416	178.9	166.4	224.230	224.070
30	9.6746	9.6746	239.7	231.0	226.380	226.377
35	9.6718	9.6731	234.1	233.7	226.183	226.277
40	9.6734	9.6737	234.4	255.1	226.296	226.318
45	9.6749	9.6712	234.8	235.2	226.405	226.143
50	9.6698	9.6719	221.9	237.8	226.046	226.193
55	9.6692	9.6696	240.8	238.4	226.004	226.030
60	9.6698	9.6706	238.9	236.4	226.045	226.101

It can be seen that the best converged value is for a kinetic energy cutoff of 30 Ry. In conclusion, being the results for the two type of mesh equal, it is meaningless to weigh down the calculations with a 6x6x6 grid.

4.1.4 Energy Cutoff Convergence

The *Kinetic Energy Cutoff* is defined as

$$E^{cut} = \frac{\hbar^2}{2m}|\vec{G}|^2 \tag{4.2}$$

where $\vec{G}$ represents the reciprocal lattice vectors. E^{cut} includes only plane-waves with energies less than this cutoff. It always has to ensure that the cutoff energy is high enough to give accurate results. The calculations are repeated, increasing the cutoff energies, until convergence is reached. In Figure 4.4 is shown, for different kinetic energy cutoff (30 Ry, 35 Ry and 40 Ry), the trends with respect to the number of $\vec{k}$-points.

It can be seen that, despite the fluctuation that arises at 35 Ry and 40 Ry, the 30 Ry graph presents a stable trend, already for 10 $\vec{k}$-points. This
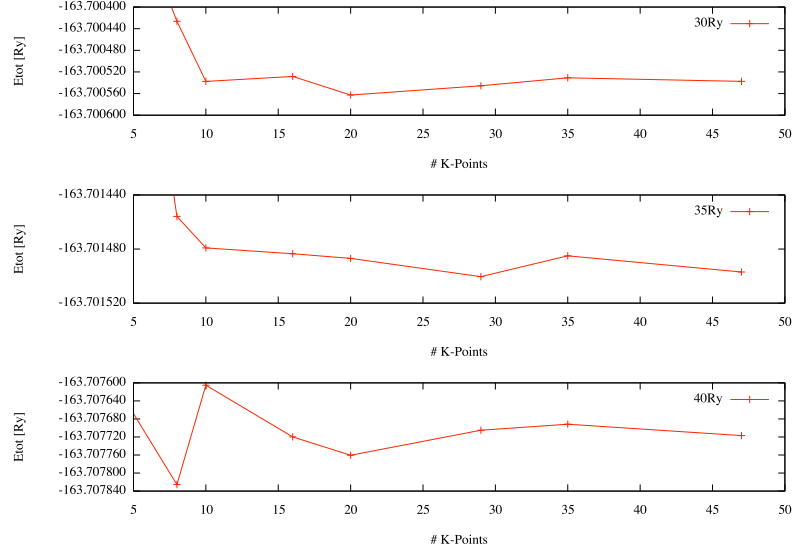
Figure 4.4: $\vec{k}$-points sampling trends compared at different energy cutoff.

is sufficient for our purpose to justify the use of a kinetic energy cutoff of 30 Ry. So, the 4x4x4 mesh and the kinetic energy cutoff of 30 Ry will be used for all the calculations reported in the following.

4.1.5 Reference

Literature comparison is necessary for gaining confidence in the calculated data. Our reference is the paper of Stapper and Parrinello[46].

In this work, authors compare the structural parameters of monoclinic, tetragonal, cubic and orthorhombic zirconia, calculated by and LDA functional. In particular, the attention is focused on the third one.

Their results are compared with the experimental data and with previous Hartree-Fock (HF) and density-functional-based (DFT) *ab initio* calculations. In this context, for our pourpose, it is necessary to evaluate just the cubic structure.

In Table 4.6 it is added the Bulk Modulus and the Volume/Atom ratio, got from the convergence tests, in comparison with the previous cited work and other papers.

Table 4.6: Data comparison between References and the present work

Phase	V/Atom [Å]	Bulk Modulus [GPa]
Cubic		
This work PBE	11.18	234.4
Paper[46]	10.91	268
Exp.	10.99 [47]	194-220[48]
Theor. HF[49]	11.41	***
Theor. DFT[50]	11.24	267
Theor. FLAPW[51]	10.76	221

It can be seen that data obtained in this work are very close to the reference[46] and to the experimental one. It means that $\vec{k}$-point grids have been set so as to solve numerically with sufficient precision the KS equations.

Chapter 5

Zirconia and Tantalia Polymorphs

Before focusing on the point defects of the novel orthorhombic Ta-doped zirconia system, we start assessing the properties and relative energies of the pure ZrO_2 and Ta_2O_5 polymorphs, and compare the results with the literature[46]. We address our attention to the monoclinic (P21/c) and orthorhombic (Pca21). Moreover we also considered the Tantalia orthorhombic phase (Pccm), structurally similar to doped zirconia crystal. In the next three sections we characterize the structural and electronic properties of these systems, corroborating results we DOS and band structure plots and crystal models used.

5.1 Monoclinic Zirconia (P21/c)

Monoclinic zirconia is the most stable zirconium oxide phase at temperature below 1170°C. The crystal structure is modeled on the basis of X-Ray Powder Diffraction data experimentally extrapolated. The monoclinic crystal is described by three unequal vectors and the β angle, different from 90°.
The two possible monoclinic crystals in the Bravais Lattices classification are:

- the primitive, (see Figure 5.1);

- the centered, (see Figure 5.2).
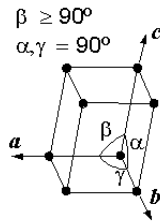
Figure 5.1: Primitive Unit Cell   Figure 5.2: Centered Unit Cell
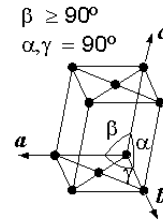
We have modeled the bulk monoclinic ZrO_2 by means of the primitive monoclinic system. Figure 5.3 shows the unit cell obtained from experimental data. Green and red spheres denote zirconium and oxygen atoms, respectively.
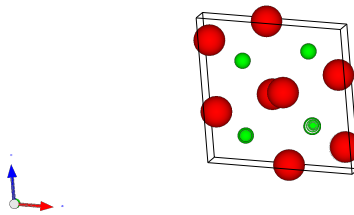
Figure 5.3: Primitive monoclinic Zirconia rebuilt on the basis of X-Ray Powder Diffraction data.

In the monoclinic structure the zirconium atoms are in a distorted sevenfold coordination, while the oxygen atoms are present both in a threefold

and fourfold coordination.

5.1.1 Structural Properties

The study and the characterization of monoclinic zirconia phase starts from considering crystallographic experimental data. The atomic positions, unit cell sides and internal coordinates are extrapolated by means of Rietveld fit refinement. Once these main crystal features are obtained, we use them for modeling the virtual monoclinic unit cell.

Thus we use the QE tool for relaxing the internal coordinates. Applying the Hellman-Feynman theorem[52], the charge density obtained from a DFT calculation can be used to obtain the forces acting on the nuclei and hence, by relaxing the forces to zero, a stable configuration is obtained.

Table 5.1 summarizes the atomic positions used for the rebuilding of the unit cell, in comparison with those used by Stapper *et al.*[46] in their work. Moreover, the experimental values which have been used as reference in the paper are compared with those extrapolated by Rietveld fit from XRD. Both simulated and experimental data are in very good agreement.

Table 5.1: Comparison in the atomic positions between this work and the References.

- Ref. [46] = experimental values as referred in the Paper of *Stapper et al.*

- Ref. [b] = experimental values from Rietveld refinement from Mestre's laboratories.

- *** = it means that there are no data available to be compared

Monoclinic Zirconia ($P2_1/c$)

	This work	*Stapper et al.*	Expt. [46]	Expt. [b]
	Zr (0.2761, 0.0434, 0.2102)	Zr (0.2769, 0.0430, 0.2100)	Zr (0.2754, 0.0395, 0.2083)	Zr (0.2777, 0.0389, 0.2086)
O^I	O1 (0.0678, 0.3312, 0.3461)	O1 (0.0640, 0.3237,0.3524)	O1 (0.0700, 0.3317, 0.3447)	O1 (0.0745, 0.3335, 0.3454)
	O2 (0.4502, 0.7574, 0.4762)	O2 (0.4497, 0.7560, 0.4790)	O2 (0.4496, 0.7569, 0.4792)	***
O^{II}	O2(0.5498, 0.2574, 0.0238)	***	***	O2 (0.5495, 0.2556, 0.0188)

Table 5.2 compares lattice parameters of *Stapper*'s work with those used in this work, relaxed and unrelaxed. The discrepancy between literature's values and those used here occurs mainly in the b/a ratio. The values obtained by cell relaxation are in good approximation with literature's.

Table 5.2: Lattice Parameters Comparison

	a	b/a	c/a	β
Ref. [46]	5.1505	1.1012	1.0234	99.230
This work [unrelaxed]	5.1428	1.0119	1.0325	99.166
This work [relaxed]	5.1780	1.0154	1.0345	99.525

The little difference can be considered negligible for the purpose of the results described in the next Section and for thermodynamical stability.

5.1.2   Electronic Properties

DOS and band structure of the equilibrated monoclinic zirconia are shown in here. The HOMO-LUMO gap is about 3.6 eV. It is known that GGA functional implemented in the pseudopotentials *underestimates* the real band gap. In Figure 5.4 we can see the different contributions to the electronic configuration of the monoclinic zirconia. The peak at -25 eV is due core
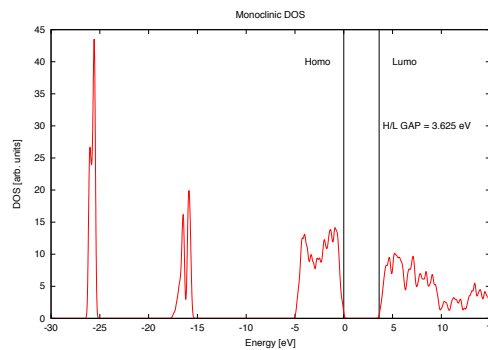
Figure 5.4: Monoclinic Zirconia Density of States

electrons belonging to the zirconium $4p$ orbitals. The double peak at $\approx$ -16 eV is the sum of two different contribution of core electrons, zirconium $5s$ orbitals and oxygen $2s$ orbitals, respectively.

Finally, valence band, immediately before the HOMO limit, is mainly made up of $2p$ oxygen orbitals and zirconium $4s$; while the conduction band, immediately after the LUMO limit, is practically composed of zirconium d orbitals only. The band gap value agrees with literature[53], which report a corresponding value of 3.16 eV . The region of interest is in the surrounding of the band gap, where the main doping effects occur.

The calculated band structure is displayed in Figure 5.5. We can observe the information reported by the DOS graph from another point of view.
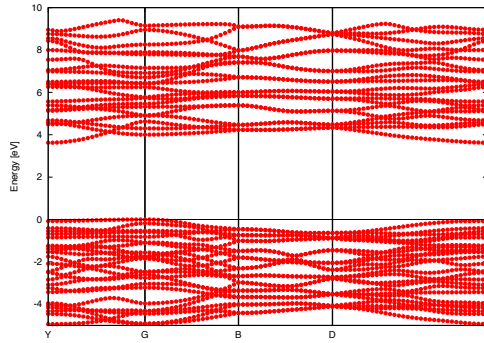
Figure 5.5: Bands Structure of Monoclinic Zirconia.

In proximity of the HOMO-LUMO gap, band structure shows if a material can be a suitable candidate to be a electron carrier or not. Monoclinic zirconia turns out to be an insulator[53]. What is clear from the analysis of the band plot is that we are dealing with an indirect band gap. It means that a contingent excited electron, in the attempt to jump from valence to the conduction band, will go through a longer path. Longer path means more possible energy profligacy.

5.2 Orthorhombic Zirconia (Pca21)

The second zirconia polymorph investigated is the orthorhombic one. The orthorhombic lattices result from cubic lattices stretching along two of the three orthogonal corners. The result is the formation of a rectangular prism with a rectangular base, with a and b, and height c, their dimensions. The

Figure 5.6: Orthorhombic Crystallographic Configurations
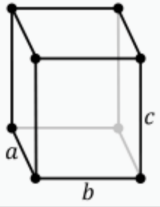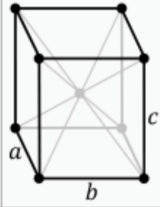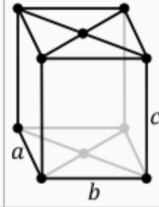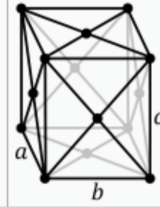
principal orthorhombic configurations, distinguishable in four classes, are reported in Figure 5.6: *Primitive*(P), *Body-Centered*(I), *Base-Centered*(A, B or C), and *Face-Centered*(F).

In this work we describe the orthorhombic phase, space group Pca21, in terms of the primitive cell, following the experimental observations.

Usually, orthorhombic zirconia could not be obtained by chemical synthesis, but it is produced by applying very high pressures and temperatures to the already existing cubic, tetragonal or monoclinic zirconia. It follows that orthorhombic zirconia is not defined by a unique space group.

5.2.1 Structural Properties

As for monoclinic zirconia, also in the study and characterization of the orthorhombic we have considered the experimental atomic positions, lattice parameters and internal coordinates, obtained by Rietveld refinement of XRD data. We consider the crystal unit cell, and also in this case, we have relaxed all structure parameters and atomic positions applying the Hellmann-Feyman theorem. Table 5.3 shows the equilibrated lattice parameters.

Table 5.3: Lattice Parameters Comparison

	a	b/a	c/a
This work [unrelaxed]	5.260	0.963	0.965
This work [relaxed]	5.308	0.959	0.964
Ref. [54]	5.220	0.961	0.966
Exp.	5.260	0.964	0.966

The values obtained are in good approximation with the reference[54]. In side a, there is a length increasing of about 0.91%.
b/a ratio presents a discrepancy with the experimental one of about 0.5%. So, data are valid and in good approximation. Table 5.4 shows experimental atomic positions used, and the same after the relaxation.

Table 5.4: Atomic Position Comparison

	This Work [relaxed]	Exp.
Zr	(0.531, 0.266, 0.249)	(0.530, 0.267, 0.250)
O1	(0.865, 0.067, 0.106)	(0.861, 0.068, 0.106)
O2	(0.228, 0.464, 0.001)	(0.229, 0.463, 0.000)

Unfortunately, the reference[54] does not report the atomic positions used and optimized, so a direct comparison cannot be done. This implies that it is necessary to rely on data extrapolated for this particular crystal structure.

Figure 5.7 and 5.8 represent the virtual reconstruction of the unit cell before and after relaxation.
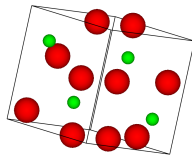
Figure 5.7: Unit Cell Unrelaxed
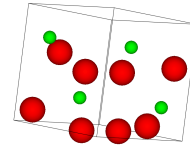
Figure 5.8: Unit Cell Relaxed

5.2.2 Electronic Properties

In orthorhombic zirconia DOS, it can be seen that the HOMO-LUMO gap is around 3.8 eV. The HOMO-LUMO gap underestimation should not be forgotten, as a consequence of the approximation implemented into the pseudopotential used. We can observe that orthorhombic DOS is quite similar to the monoclinic one.
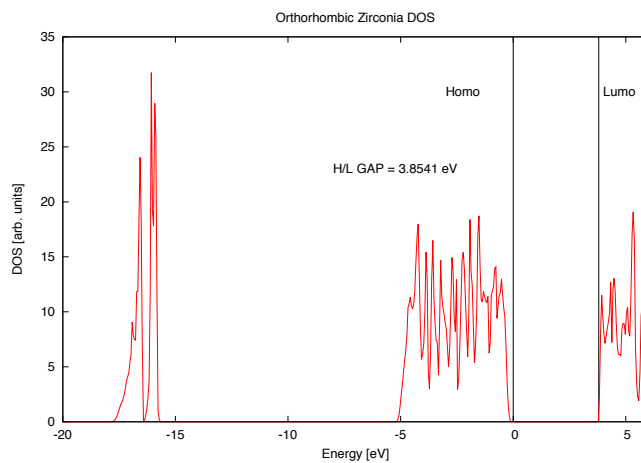
Figure 5.9: Orthorhombic Density of States

Peaks at ≈ -16 eV are very similar to those in the monoclinic DOS; also valence and conduction bands are very close to the monoclinic's. It follows that the morphological change does not have important effects on electronic

structure. As for monoclinic, the difference peaks have the same contributions from the same zirconium and oxygen orbitals. Orthorhombic zirconia band structure, Figure 5.10, is not so far from the monoclinic one. The gap between HOMO and LUMO levels are very close, and it follows that also orthorhombic zirconia is an insulator. Moreover, the same mechanism of electronic transfer, as for monoclinic zirconia, is present here, because we are dealing with an *indirect* band gap.
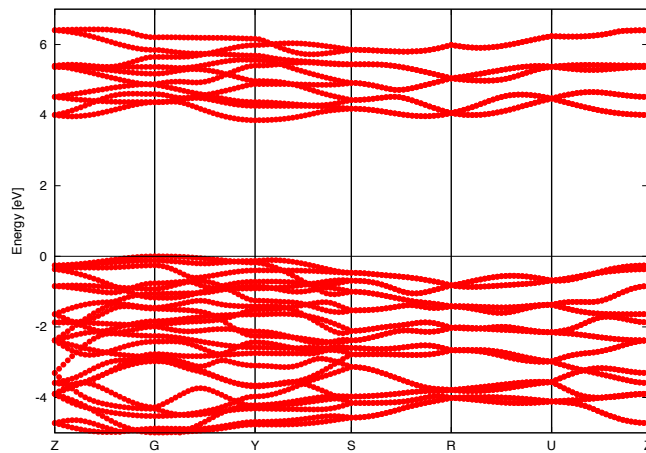
Figure 5.10: Orthorhombic Zirconia Crystallographic Configurations

In the act of planning a new semiconductor, it has to be considered which kind of path electrons will prefer to follow in operating conditions. Differently from the monoclinic zirconia, it should be take orthorhombic electronic properties with a grain of salt, because of the very little literature reference.

5.3 Orthorhombic Tantalia (Pccm)

5.3.1 Convergence Test and Lattice Parameters Selection

The ground states analysis concludes with the investigation and re-evaluation of one of the tantalum oxides polymorphs, the Orthorhombic Pccm. The aim is not just to reproduce literature[55], but also to test the pseudopotential used for Tantalum atomic species. It needs to satisfy the convergence criteria, like zirconium and oxygen pseudopotential in the cubic structure, describe in preceding Sections. The pseudopotential used is a GGA Vanderbilt ultrasoft, *Ta.pbe-nsp-van.UPF*. As in the previous cases, we use an automatic script in which we make varying at the same time the kinetic energy cutoff and the lattice parameter *a*. The other two sides are fixed.

Table 5.5: Lattice Parameters Comparison

	a	b/a	c/a
Ref. [55]	11.748	0.591	1.25
This work [converged]	12.00	0.584	1.214

Table 5.5 reports values after convergence. They are correlated to the minimum of the parabolic curve, fitted with the Murnaghan EOS. In Figure 5.11 is shown the kind of curves that are fitted. The data gained by simulation of
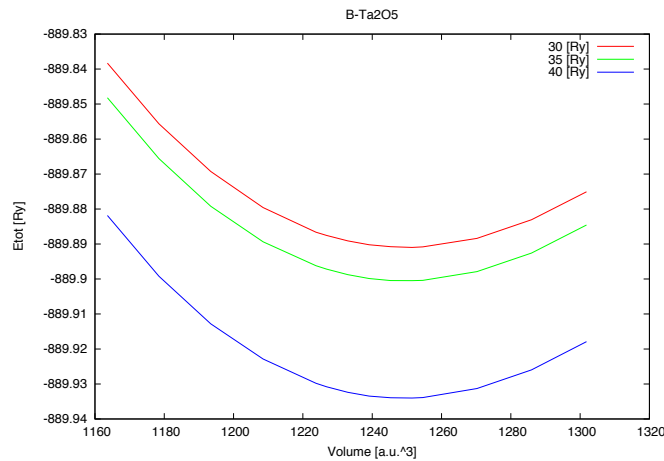
Figure 5.11: Convergence Curves

the orthorhombic tantalia are valid and in a very good approximation with Sahu *et al.*.[55] The $\vec{k}$point mesh used for every calculation was 4 8 3. Table 5.6 summarizes the bulk modulus calculated with the EOS:

Table 5.6: Bulk Modulus Comparison

Energy Cutoff [Ry]	Volume [a.u.]^3	Bulk Modulus [GPa]	Emin [Ry]
20	1249.25	218.7	-888.54
25	1249.37	226.7	-889.73
30	1249.85	231.2	-889.89
35	1249.49	229.7	-889.90
40	1249.30	231.0	-889.93
45	1248.11	228.1	-889.98
50	1247.77	229.8	-890.02
55	1247.76	229.7	-890.05
60	1247.35	229.7	-890.06

The bulk modulus obtained at 30 Ry is very close to one obtained by the paper authors, equal to 231.47 GPa.

5.3.2 Electronic Properties

The orthorhombic tantalia DOS is not uniquely determined, but it depends upon the functional adopted in the calculations. The experimental Ta_2O_5 band gap is about 4.1 eV[56].
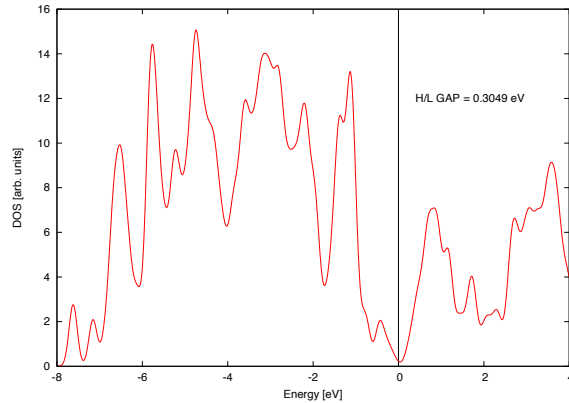
Figure 5.12: Orthorhombic Tantalia Density of States

We calculate a band gap of about 0.3 eV. This discrepancy can be filled by applying a hybrid functional like B3LYP, which involves Hartree-Fock exchange energy. We instead use the GGA pseudopotential.

In Table 5.7 we summarize the values in literature concerning the band gap of tantalia.

Table 5.7: Bulk Modulus Comparison

Structure			E_g [eV]
β-Ta_2O_5			
	This work		0.3
	Ref.	[56]	4.1
	Ref.	[57]	0.2
	Ref.	[58]	0.1
	Ref.	[59]	5.06
	Ref.	[60]	2.43
	Ref.	[61]	2.0-2.2
	exp.	[62]	4.0-4.2

Such a small band gap suggests that the orthorhombic β-tantalia is a semiconductor, but unfortunately it is just a great underestimation due to the functional used to simulate the tantalum atom. This error is present also in the band structure plot, Figure 5.13. What is wrong is the gap between HOMO and LUMO levels, but not how the bands are reported.
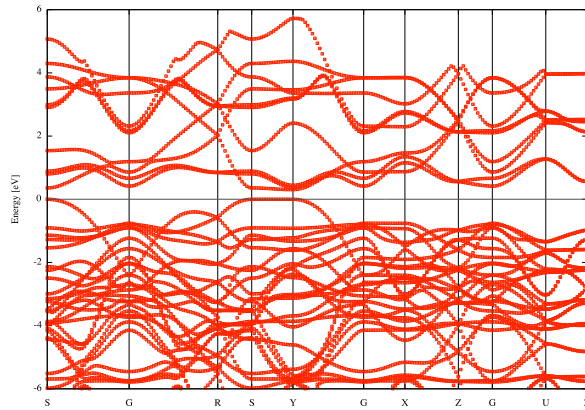
Figure 5.13: Orthorhombic Bands Structure

Nevertheless, Figure 5.13, is extremely faithful to the one reported in reference [55]. Figure 5.14 shows the orthorhombic tantalia unit cell investigated. It is made of four Ta_2O_5 molecular units.
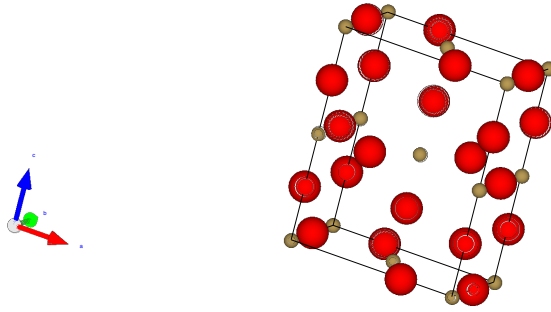
Figure 5.14: Orthorhombic Tantalia Unit Cell

The aim of testing the quality of the pseudopotential, and then the electronic properties correlated to Ta_2O_5 is reached. Results are in confidence with those of other authors. The question concerning the gap is, at this time, negligible.

5.4   Summary

The aim of accurately to reproduce literature[38][46] and structures is achieved. We started from the experimental data concerning the structural parameters of the main bulk structure, which we used for modeling the crystal unit cell. Then we applied an optimization algorithm to find the equilibrated atomic position of each atom contained in the unit cell. Finally, we calculated the total energy of each model and tested the quality of each pseudopotential used. As reported in Figure 5.15, the total energy versus the lattice parameter variation reproduces the correct energetic trend of zirconia phases.
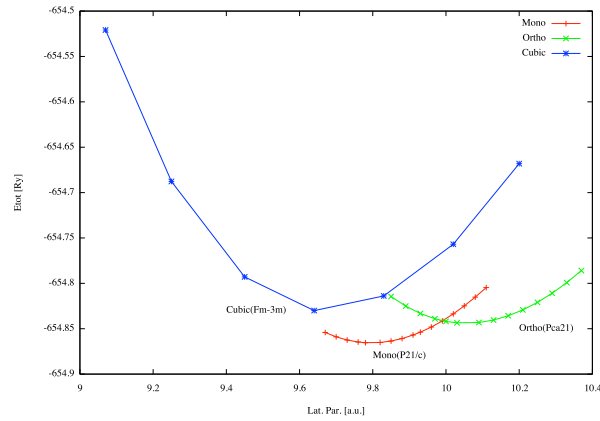
Figure 5.15: Computed energy versus lattice parameter data fitted by a Murnaghan EOS for monoclinic zirconia (red line), orthorhombic zirconia (green line), and cubic zirconia (blue line).

We can see that, as experimentally observed, that monoclinic phase is the most stable while the others two phases considered are at higher energy values. This is a very important step. The pseudopotentials are tested with satisfactory results and they correctly reproduce what are the experimental observations.

Chapter 6

Defect Chemistry of Ta-doped Zirconia

6.1   Atomistic *ab initio* Thermodynamic

We started from the structural parameters values extrapolated by XRD diffraction experiments, concerning the two main Ta-doped zirconia phases, monoclinic and orthorhombic. The measurement alone cannot determine which are the compensating defects from Ta doping. These can be electronic or crystalline (vacancies, interstitials, etc.). To provide this complementary information we took into consideration two probable defects that can contribute to the stabilization of the phases. In this work we considered the following mechanism: 1) we replace zirconium atoms with tantalum atoms and contemplate the presence of oxygen vacancies (i.e. crystalline defects), and 2) we replace zirconium atoms with tantalum atoms but without the generation of oxygen holes, (i.e. electronic defects). In both the models the supercells considered are neutral. Thus, we modeled the crystal unit cells of each principal component of the Ta-doped zirconia, starting from their molecular units, ZrO_2 and Ta_2O_5, and testing the pseudopotentials used to simulate each atomic species. The test were satisfactory, and we were able to correctly estimate the total energy versus lattice parameter variation of zirconia polymorphs. The aim of this work is to explore and describe the stabilization mechanism which occurs in the Ta-doped zirconia, and establish if it is correlated to crystalline or electronic defects. This has not yet been studied in literature. Some works[63]–[65] on the Ta-doped zirconia system

have been already published. Unfortunately, in these papers authors limit their investigation just on the possible electronic effects that a zirconium atom replaced with a tantalum one can produce, only in the monoclinic phase. The three works simply assume that the electronic defect is the most stable and do not explore structures containing other possible defects that can form when Ta is included in the ZrO_2 lattice.

On the contrary, in this work we go beyond this limitation and we consider different stoichiometries and defects, in order to define which is the most probable defect that occurs in realistic conditions of temperature and pressure. To make possible this in depth analysis, we need to use a method capable to calculate from first principles the free energy of a material: one possibility is the atomistic *ab initio* thermodynamics approach. In recent years[66]–[70] *ab initio* calculations combined with thermodynamic concepts have become an important strategy in structures stability analysis of complex materials that can involve intrinsic nonstoichiometries of the chemical compositions. *Ab initio* computations yield first-principles solutions of the Schrödinger equation without depending on empirical input.
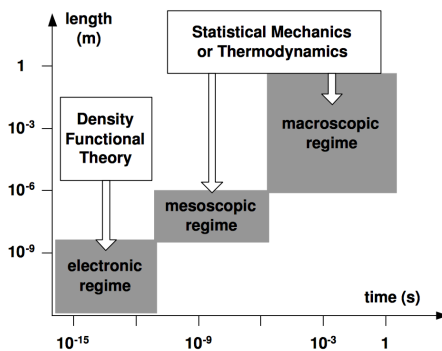
Figure 6.1: Schematic representation of the time and length scales for the micro-, meso- and macro- scopic system. It shows the methods developed in order to face problems correlated to a certain system under inverstigation.

In order to explore macroscopic phenomena on the basis of a microscopic understanding, a huge range of time and length scales need to be covered. The link between micro-, meso- and macroscopic systems is referred as *multiscale* approach. It allows for connecting total energy electronic calculations with the thermodynamics. Figure 6.1 summarizes this fundamental concept.

The computation covers a wide range of problems in surface structures[71], defect stability[72][73], doping[74] of semiconductors, oxide surfaces[75]–[78] and metal/oxide interfaces[79][80]. In the typical electronic structure calculations, the temperature and the pressure effects are not included, i.e. all evaluated physical quantities are strictly only valid at $T = 0$ K and $P = 0$ atm.

6.2   The Formalism for the Bulk Free Energy of Formation

To investigate the relative stability of bulk Zirconia (ZrO_2) under thermodynamical conditions, we have exploited an approximate scheme to calculate the bulk Gibbs free energy within a thermodynamic model, as suggested by Reuter *et al.*[68] and Bollinger *et al.*[81].

The Gibbs free energy is a thermodynamic potential state function defined as

$$G = U - TS + pV \qquad (6.1)$$

where U is the internal energy, T is the temperature, S is the entropy, p is the pressure and V is the volume. For a general crystal of zirconia, the Gibbs free energy depends on the number of zirconium atoms (N_{Zr}) and oxygen atoms (N_O) present in the sample under investigation. The most favorable thermodynamical systems at a given T and p are those that minimize the Gibbs free energy of the bulk crystalline oxide. It is possible to use total energies from DFT calculations to approximate the free energy of a system. Since we are dealing with bulk crystal solids, the pV contribution in Gibbs free energy is negligible, because the pressure value considered in standard conditions is too low to induce modifications. Thus we have

$$G \approx U - TS \qquad (6.2)$$

If we consider the zirconia system, it follows

$$G(T, V, N_{Zr}, N_O) \approx U^{tot}(V, N_{Zr}, N_O) - TS^{vib.}(T, V, N_{Zr}, N_O) \qquad (6.3)$$

where $U^{tot}(V, N_{Zr}, N_O)$ is the internal energy of the bulk zirconia; from now we rename it as $E^{tot}(V, N_{Zr}, N_O)$ for convenience.

The term $S^{vib.}(T, V, N_{Zr}, N_O)$ states for the entropic contributions. They include vibrational and configurational terms, both of them depends on the crystal configurations. In principle, the vibrational contribution can be estimated from the phonon density of states. However, given the melting temperature of ZrO_2 (2953 K), we do not consider this term. The configurational contribution due to different dopants arrangement are also neglected here. Following similar literature, in the present work the Gibbs free energy can be approximated as

$$G(T, P, N_{Zr}, N_O) \approx E_{DFT}^{tot}(T_{0K}, V_{cost.}, N_{Zr}, N_O) \qquad (6.4)$$

where in this case the $E_{DFT}^{tot}(T_{0K}, V_{cost.}, N_{Zr}, N_O)$ states for the total energy value estimated by DFT calculation.

While the capital G(T,P) denotes the Gibbs free energy of formation of the crystalline supercell, we define lowercase g(T,P) as the Gibbs free energy of the stable ZrO_2 polymorphs per molecular unit. In this thesis we focus on the thermodynamic analysis of the free energy of formation of different phases of pure and Ta-doped zirconia. In particular, for the case of zirconia, the respective Gibbs free energy of formation is

$$G^{form}(T, P) \approx n \cdot g_{ZrO_2}^{form} = n \cdot \mu_{ZrO_2} \qquad (6.5)$$

where μ_{ZrO_2} represent the chemical potential of zirconia per molecular unit, and n the number of unit per supercell. The corresponding Gibbs free energy of formation per zirconia molecular units us defined as

$$g_{ZrO_2}^{form}(T, P) = E_{tot}^{DFT} - \mu_{Zr} - 2\mu_O(T, P) \qquad (6.6)$$

where μ_{Zr} is the chemical potential of zirconium and μ_O(T,P) is the chemical potential of oxygen. If we consider Eq.(6.5), we can rewrite it in the form of Eq.(6.6) and generalized it as

$$G^{form}(T, P) = E_{tot}^{DFT} - N_{Zr}\mu_{Zr} - N_O\mu_O(T, P) \qquad (6.7)$$

Notice that the only term which depends upon temperature and pressure is the oxygen chemical potential.

6.2.1 Oxygen Chemical Potential

It is now necessary to establish the dependence of μ_O from T and P, in a gas of molecular O_2. Assuming that the gas is ideal, the dependence of oxygen chemical potential with pressure and temperature is

$$\mu_O(T, P) = \mu_O(T, P_0) + \frac{1}{2} kT \ln \frac{P}{P_0} \qquad (6.8)$$

where P_0 is the reference pressure in standard conditions ($P_0 = 0.1$ MPa)[82]. So, $\mu_O(T, P_0)$ can be decomposed into two terms

$$\mu_O(T, P_0) = \frac{1}{2} g_{O_2}^{ref}(T, P) + \frac{1}{2} \Delta g_{O_2}(T, P_0) \qquad (6.9)$$

where the first term, $g_{O_2}^{ref}(T, P)$, is the Gibbs free energy of oxygen molecule calculated in three different ways, as we will describe later. The second term, $\Delta g_{O_2}(T, P_0)$, is the entropy contribution in O_2 gas. This term has an important role in the correct evaluation of the oxygen chemical potential. It correspond to the difference in the Gibbs free energy per O_2 molecule between 0 K and T, at constant pressure P_0. It is related to the enthalpy h and entropy s as

$$\Delta g_{O_2}(T, P_0) = h(T, P_0) - h(0K, P_0) - Ts(T, P_0) \qquad (6.10)$$

The values of h and s are tabulated in the thermochemical tables[82], for different values of T and P. Although these terms could be calculated with statistical mechanic approaches, in this work we will use the tabulated experimental values. For standard conditions, these are: METTERE VALORI TABELLE NIST So, $\Delta g_O(T_0,P_0)$ per oxygen atom is

$$\Delta g_O(T_0, P_0) = \tfrac{1}{2} \left[0 - 298.15 \cdot 205.147 \right] = -30.5823 \ \tfrac{kJ}{mol} = -0.3169 \ eV$$

This term is added to the oxygen chemical potential formula, as it will shown in next Sections. The entropy calculation should takes into account also vibrational and rotational contributions, but here they are omitted.

In oder to be able to apply equations referred to G^{form}(T,P), we have to define and describe g_{O_2}(T,P). The literature[68] reports different approaches

that we will explore in the following Sections. Summarizing, g_{O_2}(T,P) can be calculated starting from the total energy of an isolated oxygen molecule, as anticipated in Eq.(6.9). Otherwise it can be estimated starting from the total energy of an isolated oxygen atom, Section 6.3.2. Finally, we can calculate the oxygen chemical potential as a function of the Gibbs free energy of formation of any oxide for which the ΔG^{form} is already experimentally known, Section 6.3.3.

In order to establish which is the most accurate choice to apply to ZrO_2, we will calculate with the three methods explain above the Gibbs free energy of formation of bulk zirconia.

6.2.2 Limits Allowed in Oxygen Chemical Potential

Pressure and temperature are variables in experimental procedures. It is convenient to consider the dependence of the atomic free energy with respect to μ_O(T,P), which carriers the only explicit dependency of the thermodynamics on T and P. If μ_O(T,P) becomes too low, all oxygen would leave the sample. It means that the oxide will decompose into solid Zr and oxygen gas. It follows that

$$max\left[\mu_{zr}(P=0)\right] \equiv g_{Zr} \tag{6.11}$$

where g_{Zr} is the Gibbs free energy of metallic zirconium, which is approximated to the total energy calculated with the DFT approach.

Eq. (6.6), in the limit of $T = 0\ K$ and $P = 0\ atm$ conditions, will employ that

$$min\left[\mu_O(T,P)\right] \equiv \frac{1}{2}\left[g_{ZrO_2}(0,0) - g_{Zr}\right] \tag{6.12}$$

marking the *Oxygen-poor limit*, or equivalently *Zr-rich limit*. It is a theoretically well-defined reference point on the μ_O axis. On the other hand, the *Oxygen-rich limit* can be defined as the point beyond which O atom from the gas phase would start to condense on the sample[69].

As defined for *Zr-rich condition*, *Oxygen-rich limit* can be defined the as follow

$$max\left[\mu_O(T,P)\right] \equiv \frac{1}{2}E_{O_2}^{total}(T,P) \tag{6.13}$$

where $E_{O_2}^{total}$ is the total energy of a free, isolated O_2 molecule at $T = 0$ K. So, the Gibbs free energy of formation of the oxide, ΔG_f(T,P), can be

defined as follow

$$\Delta G^{form}(T,P) = g_{ZrO2} - g_{Zr} - g_{O_2}(T,P) \qquad (6.14)$$

where $g_{O_2}^{gas}(T,P)$ is the Gibbs free energy of an oxygen molecule.

6.3 Calculating the Reference of Oxygen Chemical Potential

The next three Sections will deal with the methods used to correctly extrapolate the Gibbs energy of formation for monoclinic bulk zirconia, by using different approximations for the reference $g_O^{ref}(T,P)$ of Eq.(6.9) of the oxygen chemical potential. Once tested for a particular phase, it can be extended to the others polymorphs. In Sections 6.3.1 and 6.3.2 respectively, we calculate $\Delta G_{ZrO_2}^{form}$, with an oxygen chemical potential calculated from the O_2 molecule or O atom. While in the third approach, Section 6.3.3, we evaluate the oxygen chemical potential, on the basis of the experimental enthalpy of formation of bulk zirconia.

Before going into the details of defining $g_{O_2}^{ref}$(T,P), we explain how the $\Delta G_{ZrO_2}^{form}$(T,P) is calculated. In the prospective to be as much precise as possible, the evaluation of the $g_{ZrO_2}^{form}(T,P) \approx \mu_{ZrO_2} - \mu_{Zr} - \mu_O$(T,P) is carried out for two different kinetic energy cutoff. This is done in order to highlight how the choice of the cutoff can influence the results. The total energy is calculated for the oxygen molecule O_2, the oxygen atom, the bulk zirconium, and the bulk zirconia ZrO_2. The chosen zirconia phase is the most stable in standard conditions, i.e. the monoclinic. Zirconia unit cell contains four unit formula, so the total energy calculate will be divided by 4 as to refer it to a unit formula. Zirconium metallic bulk is evaluated with the usual convergence criteria, being in a hexagonal close-packed configuration. The unit cell contains two atoms, so the total energy have to divided by half of its value. Atomic oxygen and the oxygen molecule total energy are evaluated, paying particular attention to the electronic configuration. Table 6.1 shows the values obtained for the different calculations performed as stated previously.

Table 6.1: Total energy calculations. The symbol *** means that the value do not need to be divided, and so it has no values in the Fraction columns

Atomic Species	Ratio Factor	30 [Ry]	Fraction [Ry]	50 [Ry]	Fraction [Ry]
E_o^{tot}	***	-31.6604	***	-31.6765	***
$E_{o_2}^{tot}$	1/2	-63.8080	-31.9040	-63.8338	-31.9169
E_{Zr}^{tot}	1/2	-207.6281	-103.8141	-207.6341	-103.8171
$E_{ZrO_2}^{tot}$	1/4	-673.4116	-168.3529	-673.5241	-168.3810

DFT method is known to bad estimate the total energy of oxygen due to the overbinding effect introduced. So, some test on that are carried out with the aim to correctly assess its electronic configuration, in atom and molecule.

6.3.1 g_O^{ref} in Terms of E_{O_2}

The fundamental equation used for calculating $\Delta G_{ZrO_2}^{form}$ is

$$\Delta G_{ZrO_2}^{form}(T, P) = \mu_{ZrO_2} - \mu_{Zr} - 2 \cdot \mu_O(T, P) \qquad (6.15)$$

where the term μ_{ZrO_2} refers to the total energy of bulk zirconia estimated by DFT calculation, and μ_{Zr} is the total energy of bulk zirconium estimated in the same way.
The oxygen chemical potential, $\mu_O(T, P)$, is calculated as

$$\mu_O(T, P) = g_O^{ref} + \Delta g_{O_2}(T, P) \qquad (6.16)$$

where g_O^{ref} is estimated in terms of the total energy of the O$_2$ molecule

$$g_O^{ref} = \frac{1}{2} E_{O_2}(T = 0K)$$

The study of the oxygen chemical potential is carried out for two different kinetic energy cutoff, in order to visualize how they can possibly influence the oxygen binding energy estimation and the zirconia Gibbs free energy of formation. Table 6.2 shows for the two different cutoff values the respective calculated $\mu_O(T, P)$ and the estimated $\Delta G_{ZrO_2}^{form}$, with respect to the experimental value, evaluated in standard conditions, T = 298.15 K and P = 1 Atm.

Table 6.2: Oxygen chemical potentials and Gibbs free energy of formations compared. The respective ΔG^{form} (T$_0$, P$_0$) for zirconia are quite far from the experimental value. They are referred to the standard conditions.

	at cutoff 30 (Ry) [Ry]	at cutoff 50 (Ry) [Ry]	Ref.[82] [Ry]
$\mu_O(\text{T}=0)$	-31.927315	-31.940226	***
$\Delta G^{form}_{ZrO_2}(\text{T}_0, \text{P}_0)$	-0.684208	-0.683519	***
exp. (T$_0$, P$_0$)	***	***	-0.836

The O_2 binding energy is calculated as

$$BE_{O_2} = E^{tot}_{O_2} - 2 \cdot E^{tot}_O \tag{6.18}$$

where E_{O_2} is the total energy of the oxygen molecule, while E^{tot}_O is the total energy of the oxygen atom. The calculated values are listed in Table 6.3.

Table 6.3: Oxygen molecule binding energy calculated from total energy DFT put in comparison with the experimental value.

BE_{O_2}	[Ry]	[eV]
at 30 Ry	-0.4872	-6.6285
at 50 Ry	-0.4808	-6.5421
exp.	-0.3822	-5.2

We can see, both in Table 6.2 and Table 6.3, that there is a great discrepancy between experimental and calculated oxygen molecule binding energy. The reason is the overbinding that the DFT introduces in the O_2 ground state calculation. It is known to be a problem that affects the DFT approach. Thus, we can conclude that this is not a good approach to be used in atomistic *ab initio* thermodynamics calculations.

6.3.2 g_O^{ref} in Terms of E_O

As in the previous Section, here we calculated the Gibbs free energy of formation of monoclinic zirconia. The formula used is the same as before, Eq.(6.15). In this case the estimation of the oxygen chemical potential is made starting from the total energy of the oxygen atom.

$\mu_O(T, P)$ is calculated is the following way

$$\mu_O(T, P) = g_O^{ref} + \frac{1}{2} BE_{O_2} + \Delta g_O(T, P) \qquad (6.19)$$

where g_O^{ref} represents the reference of free energy calculated by DFT. In order to correct oxygen energy contribution, we have to add half of the binding energy value, $\frac{1}{2} BE_{O_2}$. This is estimated experimentally and theoretically, see Table 6.3. Finally, $\Delta g_O(T, P)$, as earlier defined, is the entropic contribution of oxygen molecule, which has to be taken into account.

Table 6.4: Comparison between Gibbs free energy of formation for bulk zirconia, calculated for two different kinetic energies cutoff. It is also reported the experimental value of ΔG^{form} (T_0, P_0)from the thermodynamical tables[82]. All the values are referred to the standard conditions.

	at cutoff 30 (Ry) [Ry]	at cutoff 50 (Ry) [Ry]	[Ry]
$\Delta G_{ZrO_2}^{form}$(T_0, P_0) (calc.BE_{O_2})	-0.684	-0.683	***
$\Delta G_{ZrO_2}^{form}$(T_0, P_0) (exp.BE_{O_2})	-0.789	-0.782	***
Exp.(T_0, P_0)	***	***	-0.836

We use both the BE values for evaluating the best $\Delta G_{Zr_O}^{form}$. The data are reported in Table 6.4.

The experimental value for the $\Delta G_{ZrO_2}^{form}[82]$($T_0$, P_0) is highlighted. We can see that the use of the experimental oxygen binding energy brings to a better approximation of the Gibbs free energy of formation.

Thus it follows that the introduction of the experimental BE_{O_2} favors better zirconia Gibbs free energy of formation results.

6.3.3 g_O^{ref} in Terms of $\Delta G_{ZrO_2}^{exp.}$

Finally, in this Section we calculate the g_O reference in terms of the experimental value of Gibbs free energy of formation of zirconia, $\Delta G_{ZrO_2}^{form}$. It helps to define precisely which is the error introduced with the DFT approach. Moreover, on the basis of that, we calculate again what is the value of the BE_{O_2}, leading to the choice of the best parameter to be used in the thermodynamical calculations. The experimental $\Delta G_{ZrO_2}^{form}$ is equal to -0.836 Rydberg. Thus, rewriting Eq.(6.15) in order to obtain $\mu_O(T,P)$ as a function of experimental $\Delta G_{ZrO_2}^{form}$, we obtain

$$\mu_O(T,P) = \frac{1}{2}\left(\mu_{ZrO_2} - \Delta G_{ZrO_2-exp.}^{form} - \mu_{Zr}\right) \tag{6.20}$$

All the terms in Eq.(6.20) are already known. It is as usual calculated for different kinetic energy cutoff at 30 and 50 Rydberg. The data are listed in Table 6.5.

Table 6.5: Oxygen chemical potentials and binding energies calculated for two different energy cutoff. The blue is the BE_{O_2} value closer to the experimental one, in red.

	at cutoff 30 (Ry) [Ry]	at cutoff 50 (Ry) [Ry]	exp. [Ry]
μ_O(T,P)	-31.8514	-31.8639	***
BE_{O_2}	-0.3819	-0.3749	-0.3822

The two oxygen chemical potentials in Table above differ by 0.0126 Ry, which correspond to $\approx$ 0.17 eV. On the basis of those data, we estimate the BE_{O_2}, calculated as follow

$$BE_{O_2} = 2\cdot\left(\mu_O(T,P) - g_O^{ref}\right) \tag{6.21}$$

where μ_O(T,P) is the oxygen chemical potential evaluated as described above, while g_O^{ref} is the reference for total energy of atomic oxygen calculated by DFT.

So, comparing g_O^{ref} calculated in terms of E_{O_2}, E_O and $\Delta G_{ZrO_2}^{exp.}$, we can establish which is the most accurate oxygen chemical potential to be used into

the thermodynamical calculations. We can exclude the values of g_O^{ref} calculated starting from E_{O_2}. They are heavily influenced by the O_2 overbinding. On the other hand, both g_O^{ref} data obtained starting from E_O and $\Delta G_{ZrO_2}^{exp.}$ well approximate what are the experimental values of $\mu_O(T,P)$ and O_2 binding energy. The difference that occurs between the $\Delta G_{ZrO_2}^{form}$ estimated in Section 6.3.2 and $\Delta G_{ZrO_2}^{exp.}$ used in Section 6.3.3 are about $\approx 5.6\%$, so they are very closed each other. We conclude that $\mu_O(T,P)$ at 30 Ry is a very good reference and we will apply it to our thermodynamical calculations.

6.4   Gibbs Free Energy of Formation of Ta-Doped Zirconia

The crystallographic phases considered in this work are the monoclinic and orthorhombic zirconia, doped with different amount of Ta_2O_5, as discussed in preceding Sections. The work is planned so that to evaluate the total energy from DFT calculation. Atomic positions of each crystal structure are relaxed[52] in order to minimize forces between atoms, thanks to the Hellmann-Feynman theorem. The crystal structures investigated are six, other than the pristine zirconia polymorphs, three for monoclinic phase and three for orthorhombic phase. The doping corresponds to the replacement of zirconium atoms with tantalum atoms. The generation of defects are taken into account as described in preceding Sections. All the crystals are considered to be neutral in order to avoid the complication of the charge to be considered into the thermodynamical equations. The doping percentage is calculated as the ratio between the number of tantalum atoms introduced and the number of zirconium atoms residual, as

$$\%Ta_2O_5 = \frac{N_{intr.}^{Ta}}{N_{res.}^{Zr}} \cdot 100 \tag{6.22}$$

The monoclinic and orthorhombic structures considered are reported in Fig-

(a) 0%   (b) 3.2%   (c) 6.6%
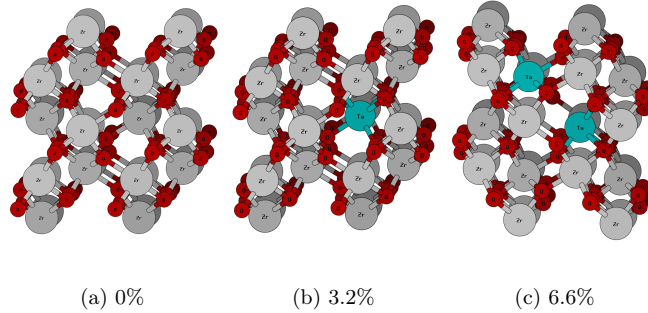
Figure 6.2: The three pictures shows the doping used in DFT calculations. Figure 7.1a is the original monoclinic supercell. Figure 7.1b is the monoclinic zirconia supercell doped with 1 tantalum atom. It is equivalent to the 3.2% of doping. Figure 7.1c is the monoclinic supercell doped with 2 tantalum atoms. Coherently to the stoichiometry one oxygen atom is removed. The doping is 6.6%. The crystals are turned in order to exhibit the doping atoms.

ure 6.2 and Figure 6.3, with respect to the ZrO_2 and ta_2O_5 stoichiometries, the resulting Ta-doped zirconia may include oxygen vacancies. To describe the thermodynamics of these solid solutions from their references we employ the following description of the composition:

$$Zr_nTa_{2m}O_{2n+5m+x} \qquad (6.23)$$

where n represents the number of zirconium atoms, $2m$ is the number of tantalum atoms and $2n+5m+x$ states for the number of oxygens of the crystal which can take into account the oxygen vacancies formation, x. Every
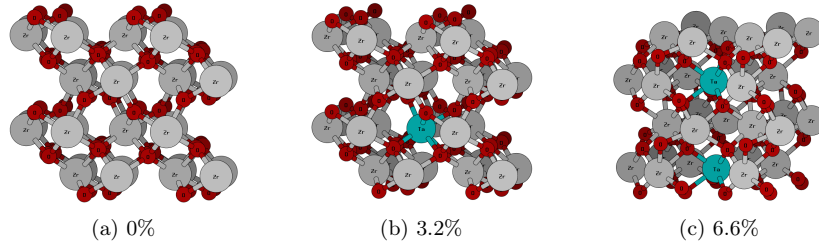

(a) 0%　　　　　　(b) 3.2%　　　　　　(c) 6.6%

Figure 6.3: The three orthorhombic crystals are shown here. In particular Figure 7.2a is the pristine orthorhombic zirconia, while Figure 7.2b and Figure 7.2c are the respective doped crystals with one atom of Ta and two atoms of Ta. The crystals are turned in order to exhibit the doping atoms.

given composition of the solid solution can be expressed using this definition, which emphasize whether it is a solid solution of stoichiometric ZrO_2 and Ta_2O_5, or if it requires an excess (or lack) of oxygen atoms (x) to compensate for the electrostatics. We have worked with a 2x2x2 fluoritic supercell containing 32 cation sites. With respect to this supercell, the compositions

Table 6.6: Stoichiometry used in the Ta-doped zirconia supercells.

	# of Zr n	# of Ta $2m$	# of O $2n + 5m + x$	excess of $O(x)$	# of vacancies in fluorite ZrO_2 2x2x2 supercell
A	31	1	64	-0.5	0.5
B	30	2	63	-2	2
C	30	2	64	-1	1
D	30	2	65	0	0

considered in this work are listed in Table 6.6. Both the monoclinic and

orthorhombic structures were considered for all the stoichiometries listed in Table 6.6. Each stoichiometry is labelled with a capital letter, A,B,C and D.

6.5 Thermodynamical Investigation

If we apply Eq.(6.15), it is possible to adapt it to the stoichiometry formulation of each bulk structure analyzed (see Figures 6.2-6.3). By substitution of the chemical potentials of each element with those per each molecule formula units, we can correctly describe how the doping affects the energies of crystals and which is the most favored to be form. The general formula to be used is

$$\Delta G_{form}(T,P) = \left(E^{tot}_{Zr_nTa_{2m}O_{2n+5m+x}} - n \cdot \mu_{ZrO_2} - m \cdot \mu_{Ta_2O_5} \right) - x \cdot \mu_O(T,P) \tag{6.24}$$

where $E^{DFT}_{Zr_nTa_{2m}O_{2n+5m+x}}$ is the total energy of each structure analyzed as in the output of the DFT calculation; $n \cdot \mu_{ZrO_2}$ and $m \cdot \mu_{Ta_2O_5}$ are the number of molecular units contained into the supercells multiplied by their relative total energies per molecular unit. Finally the term $x \cdot \mu_O(T,P)$ takes into account the eventual excess of oxygen atoms in the solid solution, multiplied by the oxygen chemical potential; it is made varying in a range of values, as described in Section 6.2.2.

A simplified form of the Eq.(6.24) is

$$\Delta G_{form}(T,P) = K - x \cdot \mu_O(T,P) \tag{6.25}$$

where K is the quantity that is calculated from the first principles. In this form, it is clear that free energy depends linearly on the chemical potential of oxygen, which in turn depend linearly on the temperature and as the logarithm of the pressure. The explicit formula for the cases A, B and C , both orthorhombic and monoclinic (we use the nomenclature A^m to express the composition A in the monoclinic structure) are:

$$\Delta G^{+1Ta}_{form}(T,P) = N \left[\left(E^{DFT}_{Zr_{31}Ta_1O_{62+2.5-0.5}} - 31 \cdot \mu^m_{ZrO_2} - 0.5 \cdot \mu_{Ta_2O_5} \right) + 0.5 \cdot \mu_O(T,P) \right] \tag{6.26}$$

$$\Delta G_{form}^{+2Ta}(T,P) = N' \left[\left(E_{Zr_{30}Ta_2O_{60+5-2}}^{DFT} - 30 \cdot \mu_{ZrO_2}^m - 1 \cdot \mu_{Ta_2O_5} \right) + 2 \cdot \mu_O(T,P) \right] \tag{6.27}$$

$$\Delta G_{form}^{+2Ta}(T,P) = N' \left[\left(E_{Zr_{30}Ta_2O_{60+5-1}}^{DFT} - 30 \cdot \mu_{ZrO_2}^m - 1 \cdot \mu_{Ta_2O_5} \right) + 1 \cdot \mu_O(T,P) \right] \tag{6.28}$$

where N and N' are the normalization coefficients, defined as the number of tantalum atoms divided by the number of zirconium atoms. $\mu_{ZrO_2}^m$ is the zirconia chemical potential referred to the most stable phase of zirconia, the monoclinic. The total energies values referred to each structure investigated are listed in the Table 6.7.

Table 6.7: Ta-doped polymorphs total energies.

	E_{tot}^m [Ry]	E_{tot}^o [Ry]
Pristine ZrO_2	-5387.633	-5387.465
A	-5425.682	-5425.502
B	-5431.405	-5431.243
C	-5463.729	-5463.542

The total energy which belongs to the pure monoclinic zirconia, divided by the total number of ZrO_2 molecules units (32) is the reference used in equations above. It is equal to -168.364 Ry.

Table 6.8: Gibbs free energies of formation normalized, referred to monoclinic supercell.

	ΔG_{form}^m [Ry]	ΔG_{form}^o [Ry]	$\Delta G_{form}^m - \Delta G_{form}^o = \Delta\Delta G_{form}$ [Ry]
Pristine ZrO_2	0	0.0053	-0.0053
A	0.5181	0.5239	-0.0058
B	4.2965	4.3073	-0.0108
C	2.1415	2.1540	-0.0125

The values of $\Delta\Delta G^{form}$, i.e. the difference between the monoclinic and orthorhombic phases free energy of formation, are also plotted as a function of the Ta concentration in Figure 6.4. Negative values indicate the stability

of the monoclinic phase. It can be seen that, in the range of concentrations considered here, the monoclinic phase is always preferred. The energetic preference, $\Delta\Delta G^{form}$ is not affected from the pure ZrO_2 case, by adding $\approx 6.7\%$ of Ta_2O_5. For this concentration, the presence of oxygen vacan-
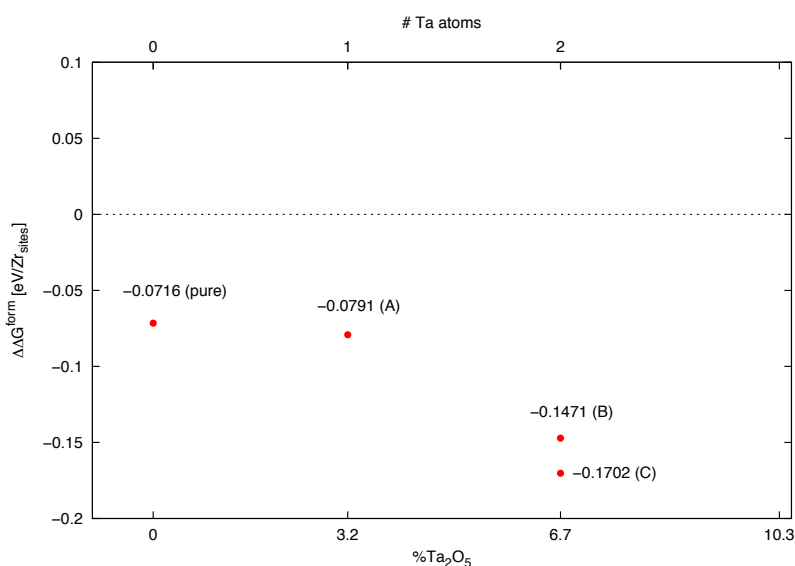

Figure 6.4: $\Delta\Delta G^{form}$ as a function of the doping content. The doping percentage and the number of Ta atoms introduced in the zirconia matrix are reported in the x-axes.

cies seems to favor the orthorhombic phase. However, in order to predict which stoichiometry, and hence which defects, is thermodynamically stable at working conditions, it is necessary to plot the phase diagram. The data reported in Table 6.8 allow for plotting a partial phase diagram only for the composition 6.7%. This is displayed in Figure 6.5 and clearly show that the system with two oxygen vacancies, despite minimizing $\Delta\Delta G^{form}$, is never more stable than the system including one oxygen vacancy. One data is running to complete this phase diagram, namely the horizontal lines corresponding to the orthorhombic and monoclinic phases for system D, that include no oxygen vacancies. The simulations are in program and will be reported in the manuscript under preparation.

This is the first complete computational study which takes into account all
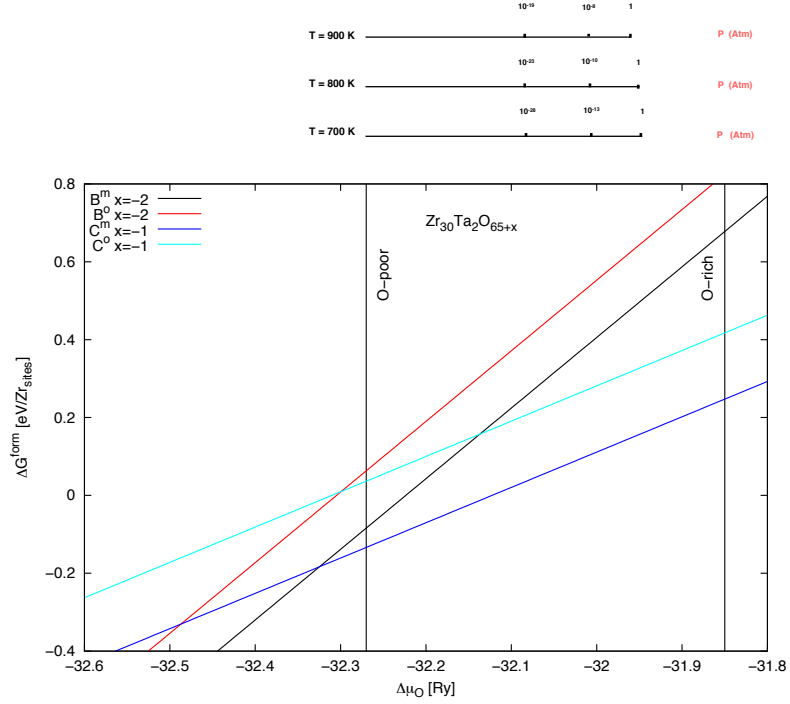
Figure 6.5: Free energy $\Delta G_{form}(T,P)$ for Ta-doped zirconia in monoclinic and orthorhombic phases as a function of the oxygen chemical potential $\Delta\mu_O$. Conversion to oxygen partial pressure P (upper axes) has been carried out at constant temperatures of T = 700, 800 and 900 K.

the main defects and their respective role in the stabilization mechanism of the Ta-doped zirconia crystal structures. The main result is that in the concentration considered in this study (3.2% and 6.7%) the most stable phases always include the presence of oxygen vacancies. Moreover, we cannot yet conclude that these are at the origin of the stabilization of the orthorhombic phase in the Ta-doped zirconia, because all our systems are predicted to be monoclinic. The systems currently under analysis, namely those including no oxygen vacancies, will complete the study and modify the preliminary conclusions indicated above.

Chapter 7

Conclusions

We started from the experimental synthesis of tantalia-doped zirconia, using the *co*-precipitation method, well-known and reliable. The powders obtained were thermally treated at about 1000 K in vacuum. It followed an in-depth analysis by X-Ray Powder Diffraction technique, in order to establish the crystalline phases in the samples synthesized. Then we analyzed the same samples at the Synchrotron Radiation Facility in Trieste by Wide Angle X-ray Scattering, in a temperature ramp. This was carried out so that to highlight the morphological changes that might occur as a function of temperature. In perspective to justify the stabilization mechanism which occurs into the orthorhombic Ta-doped zirconia, we used the atomistic *ab initio* thermodynamics approach, on the basis of the DFT calculations.

The main result is that in the concentration considered in this study (3.2% and 6.7%), the most stable phases always include the presence of oxygen vacancies. Moreover, we cannot yet conclude that these are at the origin of the stabilization of the orthorhombic phase in the Ta-doped zirconia, because all our systems are predicted to be monoclinic. The systems currently under analysis, namely those including no oxygen vacancies, will complete the study and modify the preliminary conclusions indicated above.

Chapter 8

Bibliography

[1]Science and Technology of Zirconia, edited by A. Heuer and L. W. Hobbs, Advances in Ceramics, Vol. 3.,The American Ceramic Society, Westerville, OH, 1981; Science and Technology of Zirconia II, edited by A. Heuer and L. W. Hobbs, Advances in Ceramics, Vol. 12.,The American Ceramic Society, Westerville, OH, 1984.

[2]R. Hannink, "Transformation Toughening in Zirconia Containing Ceramics," J. Am. Ceram. Soc., 87, 461-87 (2004).

[3]E. Tsalouchou, M. J. Cattell, J. C. Knowles, P. Pittayachawan, and A. McDonald, "Fatigue and Fracture Properties of Yttria Partially Stabilized Zirconia Crown Systems," Den. Mater., 24, 308-18 (2008).

[4]J. Judes and V. Kamaraj, "Preparation and Characterization of Yttria Stabilized Zirconia Minispheres by the sol-gel Drop Generation Method," Mater. Sci.: Pol., 27, 407Ð15 (2009).

[5]G. Y. Akimov, E. V. Chaika, and G. A. Marinin, "Wear and Fracture Toughness of Partially Stabilized Zirconia Ceramics Under dry Friction Against Steel," J. Frict. Wear, 30, 77-9 (2009).

[6]C. L. Yang, H.-I. Hsiang, and C. C. Chen, "Characteristics of Yttria Stabilized Tetragonal Zirconia Powder Used in Optical Fiber Connector Ferrule," Ceram. Int., 31, 297-303 (2005).

[7]H. G. Scott, "Phase relationships in the zirconia-yttria system," Journal of Materials Science, vol. 10, pp.1527-1535, 1975.

[8]M . Levin and H. F. McMurdie, Phase Diagrams for Ceramists, 1975. Edited by M. K. Reser. American Ceramic Society, Columbus, OH, Fig. 4259.

[9]N. A. Bendeliani, S. V. Popova, and L. F. Vereshchagin, "New Modifications of Zirconium Oxide and Hafnium Oxide Prepared under High Pressure" (in Russ.), Geokhimiya. 6, 617-83 (1967).

[10]Bocquillon and C. Susse, "Phase Diagram of Zirconia under Pressure" (in Fr.), Rev. Int. Hautes Temp. Refract., 6, 263-66 (1969).

[11]L. M. Lilyagina, S. S. Kabalkina, T. A. Paskina, and A. I. Khoryainov, "Polymorphism of ZrO, at High Pressures", Sov. Phys. Solid State, 20, 2009-10 (1978).

[12]R.Suyama, T. Ashida, and S. Kume, "Synthesis of the Orthorhombic Phase of ZrO", J . Am. Ceram. Soc., 68 [12] C-314-C-315 (1985).

[13]Y. Kudos, H. Takeda, and H. Arashi, "In Situ Determination of Crystal Structure for High-pressure Phase of ZrO, Using a Diamond Anvil and Single-Crystal X-ray Diffraction Method." Phys. Chem. Mineral..13,233-37 (1986).

[14]L. M. Lityagina, S. S. Kabalkina, T. A. Pashkina, and A. I. Khuzyainov, "Polymorphism of ZrO2 at High Pressures." Sov. Phys.-Solid State (Engl. Trasrl.), 20, 2009-10 (1978).

[15]H. Arashi and M. Ishigame. "Raman Spectroscopic Studies of Polymorphism in Zr02 at High Pressures,"Phys. Status Solidi (A),71,313-21 (1982).

[16]R.Suyama, H. Horiuchi, and S.Kume, "Structural Refinements of ZrO2 and HfO2 Treated at 600ąC and 6 GPa,Ó Yugyo Kyokaishi ,95, 567-68

(1987).

[17]T.K.Gupta, J.h. Bechtold, R.C. Kuznicki, L.H. Cadoff, B.R. Rossing, J. Mat. Science, 12 (1977) 2421-2426.

[18]Dent Mater. 2008 Mar;24(3):289-98. Epub 2007 Jul 12.

[19]M. Boffelli, W.Zhu, T. Francese, G. Pezzotti, Oxygen Hole States in Zirconia Lattice: Quantitative Aspects of Their Cathodoluminescence Emission, J. Phys. Chem. A, 2014, 118, 9828-9836.

[20]Fabris S, Paxton A, Finnis MW. A stabilization mechanism of zirconia based on oxygen vacancies only. Acta Mater 2002;50 : 5171- 8.

[21]Garvie RG, Nicholson PS. Structure and thermomechanical properties of partially stabilized zirconia in the CaOÐZrO2 system. J Am Ceram Soc 1972;55 (3) : 152-7.

[22]Goff JP, Hayes W, Hull S, Hutchings MT, Clausen KN. Defect structure of yttria-stabilized zirconia and its influence on the ionic conductivity at elevated temperatures. Phys Rev B 1999;59 (22):14202-19.

[23]Paye. S. E., Liopis J., Photoluminescence-Spectra Study of Yttria-Stabilized Zirconia, App. Phys. A., 57, 225-228 (1993).

[24]Paye. S. E., Liopis J., Luminescence of Polycrystalline Cubic and Tetragonal yttria-Stabilized Zircoia, J. Phys. Chem. Solids, 55, 671-676, 1994.

[25]Singh A. P., Kaur N., Kumar A., Singh K. L., J. Am. Ceram. Soc., 90, 789-796.

[26]Dauskarat R. H., David B., Ritchie R. O., J. Am. Ceram. Soc., 73, 893-903.

[27]Ma, Yanjun, and Yoshi Ono. "Zirconium or hafnium oxide doped with calcium, strontium, aluminum, lanthanum, yttrium, or scandium." U.S.

Patent No. 6,297,539. 2 Oct. 2001.

[28]Raghavan, S., et al. "Thermal properties of zirconia co-doped with trivalent and pentavalent oxides." Acta Materialia 49.1 (2001): 169-179.

[29]Tartaj, P., et al. "Origin of color in aerosol-derived vanadium-doped zirconia pigments." Journal of Mat. Res. 13.02 (1998): 413-420.

[30]P. Li, I-W. Chen, and J. E. Penner-Hahn, "Effect of Dopants on Zirconia stabilization- An X-ray Absorption Study: III, Charge-Compensating Dopants," J. Am. Ceram. Soc., 77 [5] 1289Ð95 (1994).

[31]J. C. Ray., Panda A.B., Pramanik P., "Chemical Synthesis of Nanocrystals of Tantalum Ion Doped Tetragonal Zirconia," Mater. Lett., 53 [3] 145Ð50 (2002).

[32]Richard M. Martin, Electronic Structure: Basic Theory and Practical Methods., Cambridge University Press., 2004.

[33]P. Hohenberg, W. Kohn, Phys. Rev. 136 (1964).

[34]W. Kohn, L. J Sham, Self-Consistent Equations Including Exchange and Correlation Effects*, Phys. Rev. Vol.140, A1133 (1965).

[35]M. D. Segall, P. J. D. Lindan, M. J. Probert, C. J. Pickard, P. J. Hasnip, S. J. Clark and M. C. Payne, J. Phys.: Cond. Matt. 14, 2717 (2002).

[36]M. D. Segall, J. Phys.: Condens. Matter 14, 2957 (2002).

[37]J. M. Soler, E. Artacho, J. D. Gale, A. Garcia, J. Junquera, P. Ordejon and D. Sanchez-Portal, J. Phys.: Condens. Matter 14, 2745 (2002).

[38]D. R. Bowler, T. Miyazaki and M. J. Gillan,J. Phys.: Condens. Matter 14, 2781 (2002).

[39]S. Goedecker, Rev. Mod. Phys. 71, 1085 (1999).

[40]First-Principle Molecular Dynamics, P. Giannozzi, XIX School of Pure and Applied Biophysics, Venice, 26 Jan. 2015.

[41]D.R. Hamann, M. Schlüter, and C. Chiang, Norm-Conserving Pseudopotentials, Phys. Rev. Lett. 43, 1494.

[42]Vanderbilt D., Soft self-consistent pseudopotential in a generalized eigenvalue formalism, Phys. Rev. B, 41, 7892(R), 1990.

[43]http://www.quantum-espresso.org/pseudopotentials/.

[44]Perdew, John P., Kieron Burke, and Matthias Ernzerhof. "Generalized gradient approximation made simple." Physical review letters 77.18 (1996): 3865.

[45]P. Giannozzi, S. Baroni, N. Bonini, M. Calandra, R. Car, C. Cavazzoni, D. Ceresoli, G. L. Chiarotti, M. Cococcioni, I. Dabo, A. D. Corso, S. de Gironcoli, S. Fabris, G. Fratesi, R. Gebauer, U. Gerstmann, C.Gougoussis, A. Kokalj, M. Lazzeri, L. Martin-Samos, N. Marzari, F. Mauri, R. Mazzarello, S. Paolini, A. Pasquarello, L. Paulatto, C. Sbraccia, S. Scandolo, G. Sclauzero, A. P. Seitsonen, A. Smo?? gunov, P. Umari, and R. M Wentzcovitch, J. Phys.: Condens. Matter 21, 395502 (2009).

[46]G.Stapper, M.Bernasconi, N.Nicoloso, and M. Parrinello, Phy. Rev. B, 59, 797 (1999).

[47]E. V. Stefanovich, A. L. Shluger, and C. R. A. Catlow, Phys. Rev. B 49, 11 560 (1994).

[48]P. Aldebert and J. P. Traverse, J. Am. Ceram. Soc. 68, 34 (1985).

[49]E. V. Stefanovich, A. L. Shluger, and C. R. A. Catlow, Phys. Rev. B 49, 11 560 (1994).

[50]J. K. Dewhurst and J. E. Lowther, Phys. Rev. B 57, 741 (1998).

[51]H. J. F. Jansen, Phys. Rev. B 43, 7267 (1991).

[52]Hellmann, H (1937). Einf§hrung in die Quantenchemie. Leipzig: Franz Deuticke. p. 285.

[53]Louie G. *et al.*, Structural properties and quasiparticle band structure of zirconia, Phys. Rev. B 57, 7027, (1998).

[54]Sebastian E. Reyers-Lillo, Kevin F. Garrity and Karin M. Rabe, Phys. Rev. B 90, 140103(R)(2014).

[55]B.R Sahu and Leonard Kleinman, Phys. Rev. B 69, 165202 (2004).

[56]Perevalov, T. V., and A. V. Shaposhnikov. "Ab initio simulation of the electronic structure of Ta2O5 crystal modifications." Journal of Experimental and Theoretical Physics 116.6 (2013): 995-1001.

[57]T. Gu, Z. Wang, T. Tada, and S. Watanabe, J. Appl. Phys. 106, 103713 (2009).

[58]Y.N. Wu, L. Li, and H.P. Cheng, Phys. Rev. B: Condens. Matter 83, 144105 (2011).

[59] S. Clima, G. Pourtois, A. Hardy, S. Van Elshocht, M.K. Van Bael, S. De Gendt, D. J. Wouters, M. Heyns, and J. A. Kittl, J. Electrochem. Soc. 157, G20 (2010).

[60]R. Ramprasad, J. Appl. Phys. 94, 5609 (2003).

[61]V. A. Shvets, V. S. Aliev, D. V. Gritsenko, S.S.Shaimeev, E. V. Fedosenko, S. V. Rykhlitski, V.V.Atuchin, V. A. Gritsenko, V. M. Tapilin, and H. Wong, J. Non??Cryst. Solid 354, 3025 (2008).

[62]W. H. Knausenberger and R. N. Tauber, J. Electro?? chem. Soc. 120, 927 (1973).

[63]R. E. Alonso, L. A. Errico, E. L. Peltzer y Blanca, A. Lopez-Garcia, A. Svane, and N. E. Christensen, Phys. Rev. B 78, 165206 (2008).

[64]R. E. Alonso, L. A. Errico, E. L. Peltzer y Blanca, A. Lopez-Garcia, A. Svane, and N. E. Christensen, Phys. Rev. B 82, 165203 (2010).

[65]R. E. Alonso, L. A. Errico, E. L. Peltzer y Blanca, A. Lopez-Garcia, A. Svane, and N. E. Christensen, Phys. Rev. B 85, 155202 (2012).

[66]K. Johnston, M. Castell, A. T. Paxton, and M. W. Finnis. SrTiO3(001)(2x1) recon- structions: first-principles calculations of surface energy and atomic structure com- pared with scanning tunnelling microscopy images. Physical Review B, 70:085415- 085427, 2004.

[67]M. Scheffler. Thermodynamic aspects of bulk and surface defects from first principles calculations. In Proceedings of the Fourth Symposium on Surface Physics. Studies in Surface Science and Catalisys 40, September 1987.

[68]K. Reuter and M. Scheffler. Composition, structure, and stability of RuO2(110) as a function of oxygen presssure. Physical Review B, 65:035406-035422, 2001.

[69]K. Reuter and M. Scheffler. Composition and structure of the RuO2(110) surface in an O2 and CO2 enviroment: Implications for the catalytic formation of CO2 of oxygen presssure. Physical Review B, 68:045407-045423, 2003.

[70]J. Rogal, K. Reuter, and M. Scheffler. On the thermodynamic stability of PdO surfaces. Physical Review B, 69:075421-075429, 2004.

[71]G. X. Qian, R. M. Martin, and D. J. Chadi, Phys. Rev. B 38, 7649 (1988).

[72]I. N. Remediakis, E. Kaxiras, and P. C. Kelires, Phys. Rev. Lett. 86, 4556 (2001).

[73]S. B. Zhang, and J. E. Northrup, Phys. Rev. Lett. 67, 2339 (1991).

[74]Y. Yang, S. B. Zhang, and S. T. Pantelides, Phys. Rev. Lett. 86, 5723 (2001).

[75]J. Padilla and D. Vanderbilt, Phys. Rev. B 56, 1625 (1997).

[76]X.-G. Wang, W. Weiss, Sh. K. Shaikhutdinov, R. Ritter, M. Pe- tersen, F. Wagner, R. Schlogl, and M. Scheffler, Phys. Rev. Lett. 81, 1038 (1998).

[77]X.-G. Wang, A. Chaka, M. Scheffler, Phys. Rev. Lett. 84, 3650 (2000).

[78]W. Zhang, and J. R. Smith, Phys. Rev. B 61, 16883 (2000); Phys. Rev. Lett. 85, 3225 (2000).

[79]W. Zhang, J. R. Smith, and A. G. Evans, Acta Mater. 50, 3803 (2002).

[80] I. G. Batirev, A. Alavi, and M. W. Finnis, Phys. Rev. B 62, 4698 (2000).

[81]Bollinger, M. V.; Jacobsen, K. W.; Norskov, J. K., Phys. Rev. B 2006, 67, 085410.

[82]M. W. J. Chase, NIST-JANAF Thermochemical Tables, fourth ed., American Institute of Physics, New York, (1998).

[83]Rogal J. *et al.*, Perspectives on point defect thermodynamics, Phys. Status Solidi B, 251, 1, 97-129 (2014).

Appendix A

Definitions and Technical Details

A.1 Bulk Modulus Definition

The Equation of State is a formidable means to extrapolate physical quantities by fitting data. It depends upon pressure and temperature. The stable structure at a given T and P determines all the other properties. The fundamental quantities are the energy E, pressure P and bulk modulus B, defined as

$$E = E(\Omega) \equiv E_{total}(\Omega) \tag{A.1}$$

$$P = -\frac{dE}{d\Omega} \tag{A.2}$$

$$B = -\Omega\frac{dP}{d\Omega} = \Omega\frac{d^2E}{d\Omega^2} \tag{A.3}$$

and higher derivatives of the energy. All quantities are for a fixed number of particles and E is the energy per cell of volume Ω.

A.2 Script Used

This is an example of the script used, in which is made varying at the same time the cell sides and the k-point sampling:

```
#!/bin/tcsh
foreach k ( 2 3 4 5 6 7 8 9 10 )
foreach a (9.07 9.25 9.45 9.64 9.83 10.02 10.20)

    cat > file.in << EOF
&CONTROL
calculation = "scf",
prefix = "filename",
pseudo_dir = "/pseudo/",
outdir = "./tmp/",
⋮
ATOMIC_POSITIONS alat
Zr  0.00  0.00  0.00
O  0.25  0.25  0.25
O  0.75  0.75  0.75
K_POINTS automatic
$k $k $k 0 0 0
EOF ./pw.x < file.in > file.out
end end exit0
```

It follows a fit made with an Equation of State, which lets to extrapolate physical properties like the bulk modulus, in order to compare them with literature references.

A.3 Cineca Eurora

Funded by PRACE 2IP, the project Eurora aimed at evaluating new architectures for the next generation Tier 0 systems. Eurora is the result of the collaboration between Eurotech and Cineca and the prototype, currently equipped with NVIDIA accelerators, is available to the members of PRACE and to the major Italian research entities. Eurora enables scientists to advance research and discovery across a range of scientific disciplines, including QCD, material science, astrophysics, life science, earth science and weather forecast.

Technical References:

- Architecture: 1 rack

- Model: Eurora prototype

- Processor Type: Xeon SandyBridge

- Computing Cores: 1024

- Computing Nodes: 64

- RAM: 16GByte DDR3 1600MHz per node

- Internal Network:1 FPGA (Altera Stratix V) per node, IB QDR interconnect, 3D Torus interconnect

- Disk Space: 160GByte SSD per node

- Sustained Performance: 3.150MFlop/w

Acknowledgements